JACS
JOURNAL OF THE AMERICAN CHEMICAL SOCIETY
pubs.acs.org/JACS
Article

Transuranium Sulfide via the Boron Chalcogen Mixture Method and Reversible Water Uptake in the NaCu*TS*$_3$ Family

Anna A. Berseneva, Vladislav V. Klepov, Koushik Pal, Kelly Seeley, Daniel Koury, Joseph Schaeperkoetter, Joshua T. Wright, Scott T. Misture, Mercouri G. Kanatzidis, Chris Wolverton, Artem V. Gelis, and Hans-Conrad zur Loye*

Cite This: *J. Am. Chem. Soc.* 2022, 144, 13773−13786
Read Online
ACCESS | Metrics & More | Article Recommendations | Supporting Information

ABSTRACT: The behavior of 5f electrons in soft ligand environments makes actinides, and especially transuranium chalcogenides, an intriguing class of materials for fundamental studies. Due to the affinity of actinides for oxygen, however, it is a challenge to synthesize actinide chalcogenides using non-metallic reagents. Using the boron chalcogen mixture method, we achieved the synthesis of the transuranium sulfide $NaCuNpS_3$ starting from the oxide reagent, NpO_2. Via the same synthetic route, the isostructural composition of $NaCuUS_3$ was synthesized and the material contrasted with $NaCuNpS_3$. Single crystals of the U-analogue, $NaCuUS_3$, were found to undergo an unexpected reversible hydration process to form $NaCuUS_3{\cdot}xH_2O$ ($x \approx 1.5$). A large combination of techniques was used to fully characterize the structure, hydration process, and electronic structures, specifically a combination of single crystal, powder, high temperature powder X-ray diffraction, extended X-ray absorption fine structure, infrared, and inductively coupled plasma spectroscopies, thermogravimetric analysis, and density functional theory calculations. The outcome of these analyses enabled us to determine the composition of $NaCuUS_3{\cdot}xH_2O$ and obtain a structural model that demonstrated the retention of the local structure within the $[CuUS_3]^-$ layers throughout the hydration−dehydration process. Band structure, density of states, and Bader charge calculations for $NaCuUS_3$, $NaCuUS_3{\cdot}xH_2O$, and $NaCuNpS_3$ along with X-ray absorption near edge structure, UV−vis−NIR, and work function measurements on $ACuUS_3$ (A = Na, K, and Rb) and $NaCuUS_3{\cdot}xH_2O$ samples were carried out to demonstrate that electronic properties arise from the $[CuTS_3]^-$ layers and show surprisingly little dependence on the interlayer distance.

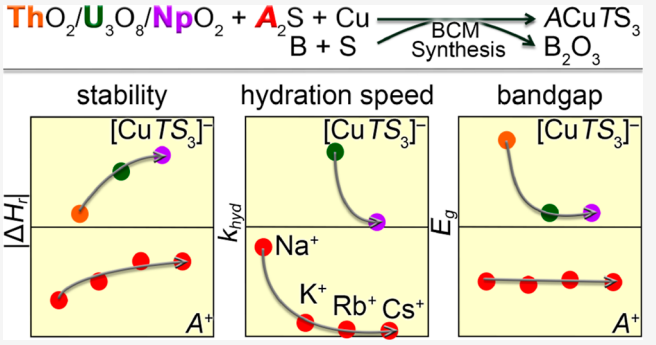

INTRODUCTION

Actinide chalcogenides are an intriguing class of compounds with extensive compositional and structural diversity that, due to the presence of 5f electrons, exhibit a wide variety of exotic physical properties.[1−22] The 5f electrons occupy an intermediate position between the more itinerant 3d and the more localized 4f electrons, resulting in the complex behavior of 5f electrons with respect to bonding to the surrounding atoms. This feature of the actinide elements plays a critical role in the reaction chemistry of the actinides as well as in the fundamental properties of actinide compounds, some of which exhibit superconductivity and complex magnetism.[23−30] Due to the actinide contraction across the actinide series, the hardness of the actinide elements increases, making their compounds with soft bases, such as chalcogenides, less favorable compared to oxide compositions.[31,32] This increasing oxophilicity creates additional challenges for the synthesis of actinide chalcogenide compounds, aside from the general increase in the radioactivity (shorter half-lives) of the heavier elements. This increased difficulty in synthesizing actinide containing compounds is reflected in the number of reported structures across the actinide series: there are 131 and 590 inorganic crystal structures of thorium and uranium chalcogenides, respectively, 79 for neptunium and plutonium chalcogenides, and only 29 combined for americium, curium, berkelium, and californium chalcogenides (Figure S1).[4,6,33−36] While the radiotoxicity of transuranium elements is inherent to them, the development of novel synthetic techniques can overcome issues related to the use of oxygen- and moisture-sensitive starting reagents and open new avenues for the synthesis and investigation of transuranium compounds.

The selection of starting materials for the synthesis of complex transuranium chalcogenides has been mostly limited

Received: May 4, 2022
Published: July 21, 2022

Scheme 1. NaCuTQ_3 Family of Layered Actinide Materials: (Left) Reaction Profiles via BCM Synthesis, (Middle) Unexpected Water Uptake for NaCuUQ_3 Compounds, and (Right) Electronic Structure of NaCuTS_3

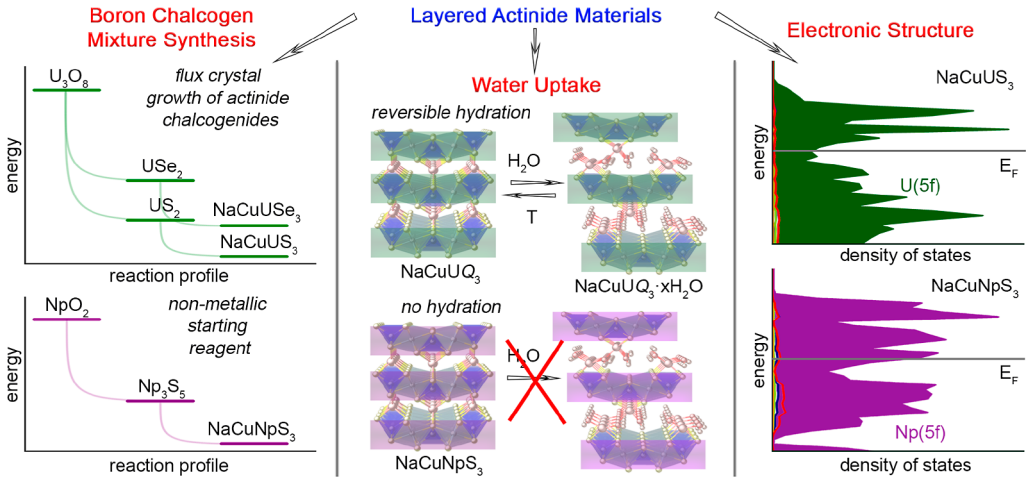

to the use of metals and, to a significantly lesser extent, binary chalcogenide reagents.[35,37,38] Both are technically and synthetically challenging due to the ubiquitous presence of surface oxygen that can lead to the formation of oxychalcogenide and/or even oxide impurities.[39−46] This issue is exacerbated by the fact that most radioactive material gloveboxes operate at negative pressures to contain highly radioactive materials, albeit at the expense of atmosphere inertness.[47−50] Oxygen and moisture readily react with actinide metals and their chalcogenides, throwing off stoichiometries of the reactions and introducing impurity products that impact the measurement of the physical properties of the target phases. To avoid this issue, new synthetic techniques that uses air-stable nonhygroscopic starting materials, such as actinide oxides, are desirable. We recently demonstrated a new convenient way to synthesize binary and complex uranium and thorium chalcogenides using stable ThO_2 and U_3O_8 precursors.[51,51] The boron chalcogen mixture (BCM) method uses a mixture of elemental boron and chalcogen (sulfur, selenium, or tellurium) and utilizes boron as a sacrificial reagent to extract oxygen by forming the thermodynamically stable B_2O_3 oxide, leaving thorium or uranium to react with the chalcogen (B_2O_3 is subsequently removed by dissolution in water or methanol). The BCM method has been successfully used to convert many p-, and d-metal and lanthanide oxides to their chalcogenides, demonstrating that it can be successfully employed with nearly all metal oxides in the periodic table, except (so far) for transuranium elements,[51−55] for which the applicability of this method has not yet been established. The challenges in transuranium chalcogenides synthesis motivated us to test the applicability of the BCM method to neptunium containing chalcogenides by predicting the reaction outcome using computational thermodynamic data of the known binary actinides and by targeting the synthesis of a complex neptunium quaternary chalcogenide.

To probe the applicability of the BCM method for synthesizing Np-based chalcogenides, we selected the $AMTQ_3$ family of compounds that crystallize in the $KCuZrS_3$ structure type.[56,57] The structure of the quaternary $AMTQ_3$ chalcogenides consists of $[MTQ_3]^{n-}$ layers separated by the A^{n+} metal cations (Figure 1). The layers contain TQ_6 octahedra that connect via corner- and edge-sharing along the *c*- and *a*-directions, respectively, to generate a rectangular net framework whose voids contain the MQ_4 tetrahedra. The layers are extremely tolerant to different sizes and charges of the cations, and therefore over 150 members of the extended $AMTQ_3$ family are known.[36] The members fall into three distinct groups exhibiting specific cation charge combinations: $A^+M^+T^{4+}Q_3$ (type I), $A^{2+}M^+T^{3+}Q_3$ (type II), and $A^+M^{2+}T^{3+}Q_3$ (type III). Additional motivation was provided by the fact that several actinide compounds in this family, for example, $ACuNpS_3$ (A = K, Rb, and Cs), were computationally identified as potential candidates for topological materials,[58] making their synthesis desirable for future property measurements. Only one Na^+ cation containing member of this family has been reported so far,[59] prompting us to choose $NaCuThS_3$, $NaCuUS_3$, and $NaCuNpS_3$ as our first target compositions. The target phases NaCuTS_3 (T = Th, U, and Np) contain Na^+, Cu^+, T^{4+}, and S^{2-} ions and are type I compounds of the $AMTQ_3$ family. The series of actinide chalcogenides NaCuTS_3 would allow us to assess the stability of these phases from a crystallographic and thermodynamic standpoints, and subsequently attempt their synthesis to validate the theoretical predictions.

Herein, we report on the successful application of the BCM method to the synthesis of the transuranium chalcogenide, $NaCuNpS_3$, starting with NpO_2 using a convenient synthetic procedure that uses all oxygen stable starting material. As shown in Scheme 1, overall comparison of thermodynamic and water stability as well as electronic properties between neptunium and uranium analogues is reported. The calculated electronic structures and new convenient synthetic procedures for these materials open an avenue for new topological materials based on 5f elements.

RESULTS AND DISCUSSION

Synthesis of $NaCuNpS_3$. Before synthesizing the transuranium analogue, we explored the synthesis of $ACuThQ_3$ and $ACuUQ_3$ (A = Na, K, Rb, and Cs; Q = S and Se) to probe the stability of the A/Th and A/U-containing phases in this family. Our previous studies demonstrated that polychalcogenide flux crystal growth can be successfully coupled with the BCM method to obtain single crystals of the desired sulfide products.[35,51,60−65] A reaction between ThO_2/U_3O_8, Cu, A_2CO_3, B, and S/Se (see experimental section for more details) resulted in metallic black plate-shaped crystals of

https://doi.org/10.1021/jacs.2c04783
J. Am. Chem. Soc. 2022, 144, 13773−13786

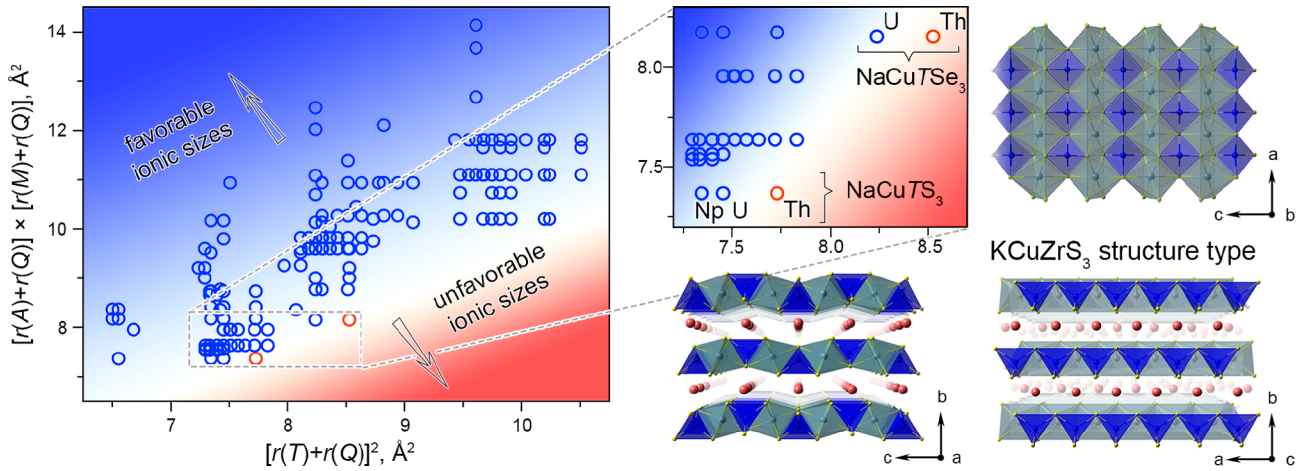

Figure 1. (left) Phase diagram of the $AMTQ_3$ compounds plotted as $[r(A) + r(Q)] \times [r(M) + r(Q)]$ vs $[r(T) + r(Q)]^2$. Blue and red points correspond to $AMTQ_3$ compounds with the $KCuZrS_3$ structure type and the potential $AMTQ_3$ compositions which we could not synthesize, respectively. The background color gradient is added to guide the eye. (right) View of the $AMTQ_3$ structure with the $KCuZrS_3$ structure type along [010], [100], and [001] directions. Pink and yellow spheres, blue tetrahedra, and gray octahedra represent *A* cations, *Q* atoms, MQ_4, and TQ_6 polyhedra, respectively.

$ACuThS_3$ or $ACuUQ_3$ (Table 1). It is worth mentioning that this synthesis of $NaCuUSe_3$ crystals represents the first example of flux crystal growth of an actinide selenide using the BCM method. On the other hand, our multiple attempts to synthesize $NaCuThS_3$ and its Se analogue only led to the formation of Th_2S_5/$ThSe_2$ and CuQ instead of the desired target phase (Figure S13). Considering that our preliminary experiments had shown the dependance of product formation on the size of the *T* cation, we performed a more detailed analysis of crystallographic and thermodynamic factors that govern the stability of the phases in the $AMTQ_3$ family to predict the stability of Np analogues.

Apart from electronic structure differences between various combinations of *A, M, T* cations, and *Q* anions, size factors often play an important role in the ability of a structure to accommodate specific elements. For example, although the size difference between six coordinate U^{4+} and Th^{4+} is as small as 0.05 Å, it is often sufficient to place an element out of the size range where it can be accommodated by a specific structure.[66] To explore the influence of cation size on phase formation in the $AMTQ_3$ family, we generated a structure adapted radius ratio plot using $[r(A) + r(Q)] \times [r(M) + r(Q)]$ vs $[r(T) + r(Q)]^2$, which was derived by Atuchin and co-workers[67,68] via machine learning (see Supporting Information, for more details, Figure S31 and Table S12) to help explain the inability of $NaCuThQ_3$ to form (Figure 1) A shift from U^{4+} to the bigger Th^{4+} cations fits the trend[67,68] that the formation of $AMTQ_3$ compounds becomes less favorable for larger $r(T)$ cations. Going from Th to U and, finally to Np, the 6-coordinate radius of T^{4+} decreases (0.94, 0.89, and 0.87 Å, respectively) and hence changes in ionic radii should stabilize compositions in the order $NaCuThS_3$ < $NaCuUS_3$ < $NaCuNpS_3$, ultimately favoring the formation of $NaCuNpS_3$.

To assess the stability of compounds in the $NaCuTS_3$ (*T* = Th, U, and Np) series from a thermodynamic perspective and to determine potential reaction sequences, we calculated the 0 K enthalpies of formation of the target products and potential binary intermediates. First, we estimated the energetics of the conversion of transuranium oxides to chalcogenides (reaction 1) and oxychalcogenides (reaction 3), as both products can

Table 1. Crystallographic Data for $ACuTQ_3$ (s.g. *Cmcm*, *Z* = 4)

compound	*a*, Å	*b*, Å	*c*, Å	R_1/wR_2, %
$NaCuUS_3$	3.9238(1)	12.7933(4)	10.2683(3)	1.35/3.66
$NaCuNpS_3$	3.9183(14)	12.813(5)	10.240(4)	2.82/7.03
$KCuThS_3$	4.0762(3)	13.8459(12)	10.5284(9)	2.53/5.74
$RbCuThS_3$	4.0890(1)	14.4515(4)	10.5319(3)	0.97/2.27
$CsCuThS_3$	4.10200(1)	15.2263(4)	10.5494(3)	1.09/2.53
$NaCuUSe_3$	4.0481(4)	13.4073(14)	10.6008(10)	3.16/8.20

form during a reaction between BCM and the reagent oxide (Figure 2)[51]

$$TO_2 + 4/3B + mQ \rightarrow TQ_m + 2/3B_2O_3 \quad (1)$$

$$\Delta H_{r1} = \Delta H_f^{0K}(TQ_m) + n/3\Delta H_f^{0K}(B_2O_3) - \Delta H_f^{0K}(TO_2) \quad (2)$$

$$TO_2 + 2/3B + mQ \rightarrow TOQ_m + 1/3B_2O_3 \quad (3)$$

$$\Delta H_{r2} = \Delta H_f^{0K}(TOQ_m) + 1/3\Delta H_f^{0K}(B_2O_3) - \Delta H_f^{0K}(TO_2) \quad (4)$$

ΔH_{r1} and ΔH_{r2} were calculated using ΔH_f^{0K} of the binary compounds from open quantum materials database (OQMD) and are shown in Figure 2 and Tables S13 and S14.[69,70] Unlike uranium and thorium oxides, for which BCM conversion to sulfides and selenides is thermodynamically favorable, neptunium oxide NpO_2 can only be converted to binary sulfides, but not to the calculated selenides and tellurides. According to calculations, the most stable neptunium sulfides are Np_2S_3 ($NpS_{1.5}$) and Np_3S_5 ($NpS_{1.6}$), which is in agreement with experimental results: sulfur-rich NpS_3 is stable below 500 °C and decomposes to Np_3S_5 above that temperature; Np_3S_5 converts to Np_2S_3 at 900 °C (Scheme S1).[37] Notably, when moving further across the actinide series to plutonium, the overall thermodynamic stability significantly increases for Pu-chalcogenides (Figure 2), suggesting that all Pu-chalcogenides can be obtained via the BCM method starting from PuO_2. While assessing the applicability of the BCM method for the

https://doi.org/10.1021/jacs.2c04783
J. Am. Chem. Soc. 2022, 144, 13773−13786

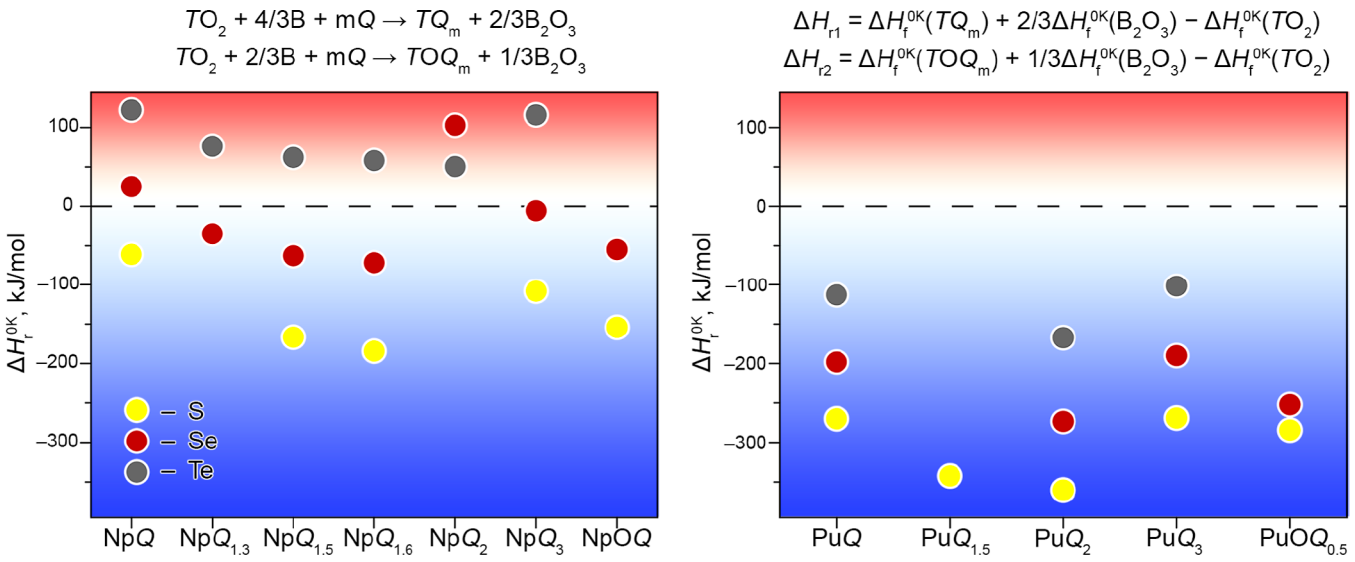

Figure 2. Enthalpies of reaction 1 and 3 for obtaining binary transuranium chalcogenides and oxychalcogenides. The formation of the phases below the dashed line is enthalpically favorable. The background color gradient is added to guide the eye. ΔH_r were estimated using calculated ΔH_f^{0K} values from OQMD.[69,70] Sulfide, selenide, and telluride phases are shown with yellow, red, and gray points, respectively.

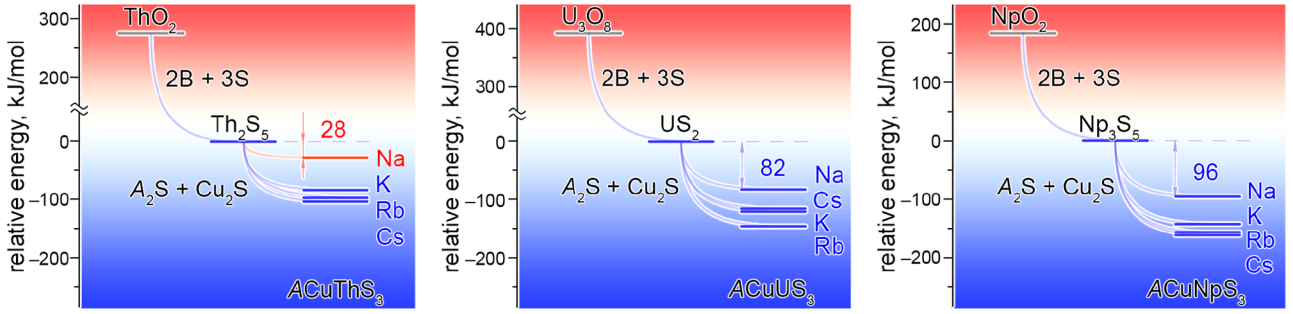

Figure 3. Relative enthalpies of the reactions 1 and 5 for $ACuTS_3$ compounds (A = Na, K, Rb, and Cs; T = Th, U, and Np).[71−73] All enthalpies of reaction are calibrated relative to reaction 1. Blue and red lines highlight experimentally accessible and non-accessible $ACuTS_3$ compositions, respectively. The background color gradient is added to guide the eye.

later actinides is hindered by a lack of computational data on the binary chalcogenides in the OQMD, one can estimate that this method can be used to form at least sulfides and selenides of Th, U, Np, and Pu.

Although successful oxide to chalcogenide conversion is a prerequisite for $NaCuTS_3$ formation, the target phase may not be thermodynamically stable. To achieve a better understanding of the thermodynamic factors (if any) that prevent the formation of $NaCuThS_3$ and allow the formation of $NaCuUS_3$, we also calculated the enthalpies of the reactions that lead to the formation of $NaCuTS_3$ phases starting from the binary chalcogenides according to the equations:

$$TS_m + 1/2Cu_2S + (2 - m)S + 1/2A_2S \rightarrow ACuTS_3 \quad (5)$$

$$\Delta H_{r3} = \Delta H_f^{0K}(ACuTS_3) - \Delta H_f^{0K}(TS_m) - 1/2\,\Delta H_f^{0K}(Cu_2S) - 1/2\Delta H_f^{0K}(A_2S) \quad (6)$$

where TS_m are stable intermediate sulfides US_2, Th_2S_5, and Np_3S_5 (Figure 3). As a matter of fact, all compounds considered in this work are stable according to convex hull analysis in the OQMD.[69,70] The enthalpies of reaction 5 for all known $ACuTS_3$ compounds (A = Na, K, Rb, and Cs; T = Th, U, and Np)[71−73] are in good agreement with our experimental observations. Figure 3 shows the reaction energy landscape for the conversion of oxides to binary and quaternary sulfides, taking the binary sulfides as a reference point, offering a visual guide of phase stability in these systems. The formation of all except one quaternary compound is strongly thermodynamically favorable with ΔH_{r3} lower than −82 kJ/mol (Tables S15 and S16). In contrast with the rest of the $ACuTS_3$ series, the least thermodynamically stable compound, $NaCuThS_3$, shows a significantly higher ΔH_{r3} of −28 kJ/mol (Tables S15 and S16), indicating that its formation may be hindered by the stability of the competing Th_2S_5 binary phase. The same trend holds true for the $ACuTSe_3$ series (A = Na, K, and Cs; T = Th and U),[74−76] where ΔH_{r3} for $NaCuUSe_3$ and $NaCuThSe_3$ are equal to −85 and −53 kJ/mol, respectively (Figure S32 and Tables S17 and S18). These results agree very well with our experimental findings that $NaCuThQ_3$ did not form and resulted in a mixture of Th_2S_5/$ThSe_2$ and CuQ (Q = S and Se) instead. These calculations also support that the formation of the $NaCuNpS_3$ phase is thermodynamically very likely, affirming $NaCuNpS_3$ as a good candidate to test the BCM method for the synthesis of a new transuranic compound.

Since the thermodynamic calculations and preliminary experiments showed that the formation of $NaCuNpS_3$ from NpO_2 oxide using the BCM method is favorable, we performed its synthesis. The reaction, which was scaled down propor-

https://doi.org/10.1021/jacs.2c04783
J. Am. Chem. Soc. 2022, 144, 13773−13786

tionally to using 6 mg of NpO_2 as a starting material along with Cu, Na_2CO_3, B, and S, yielded metallic black plate-shaped crystals of $NaCuNpS_3$. Crystals were isolated by dissolving the polychalcogenide flux in water (see Experimental Section for more details). Single crystal diffraction revealed (Table 1) that $NaCuNpS_3$ is isostructural to $NaCuUS_3$ and exhibits the actinide contraction with slightly shorter Np−S bonds, 2.6940(17)−2.7385(14) Å, compared to U−S bonds, 2.7006(6)−2.7445(4) Å (Table S4). A bond valence sum (BVS) analysis resulted in a BVS of 3.97,[72] close to the +4 that is expected for Np in $NaCuNpS_3$ (Table S8). Overall, this work demonstrates that size considerations, crystal chemical reasoning, and thermodynamic estimations based on computational enthalpies of reaction, respectively, are an effective approach for predicting phase formation in the actinide systems, including predicting the suitability of synthetic routes, such as the BCM method, that convert oxide reagents to complex chalcogenide products. This conclusion is validated by the first synthesis of $NaCuNpS_3$ using the BCM method, offering a new convenient synthetic route for the synthesis of new transuranium chalcogenides.

Hydration of $NaCuUS_3$. During the optimization of the synthetic procedure for $NaCuUS_3$, we noticed that the choice of solvent for post-reaction flux dissolution affected the final products that were isolated from different reactions performed under otherwise identical reactions conditions. When we used DMF, black plate-shaped crystals of $NaCuUS_3$ (*Cmcm* space group, Figure 4) with unit the cell parameters a = 3.92380(10) Å, b = 12.7933(4) Å, and c = 10.2683(3) Å (Table 1) were obtained. However, the use of water led to similar looking crystals that crystallized in the *P*2/*m* space group with a different set of unit cell parameters, a = 9.397(3) Å, b = 3.9050(13) Å, c = 10.235(3) Å, and β = 102.943(14)° (Table 2). Even though the diffraction quality of the latter crystals was poorer than those of $NaCuUS_3$, single crystal X-ray diffraction (SCXRD) experiments revealed the presence of $[CuUS_3]^-$ layers (Figure 4) that are separated by electron density that could not be unambiguously assigned to specific atoms. The layer structure of the water-treated crystals is nearly identical to that observed in the DMF-treated ones, in which $[CuUS_3]^-$ layers are separated by the Na^+ cations. However, between these two structures there is a significant difference in the interlayer distance, which increases from 6.40 Å in $NaCuUS_3$ to 9.16 Å for water-treated crystals (Figure 4). In light of our recent discovery of reversible hydration of $NaGaS_2$ crystals that is accompanied by a similar process (see Supporting Information for more details, Table S19 and Figure S35),[77,78] we studied the effect of the solvent on post-synthetic modifications more closely.

To understand whether there is single-crystal-to-single crystal (SCSC) hydration conversion of the $NaCuUS_3$ crystals, we soaked single crystals in water and studied the product with single crystal and powder XRD (PXRD, Figure S11). Both methods revealed that the transformation is accompanied by an increase in the interlayer distance by 2.76 Å, indicating water uptake leading to a SCSC conversion. To confirm the presence of water, we collected an infrared spectrum of the hydrated compound. A sharp absorption band at around 1600 cm^{-1} and a broad peak at 3300 cm^{-1} in the spectrum correspond to H_2O bending and O−H group stretching modes, respectively (Figure S27). The absence of extraneous elements was confirmed by energy-dispersive spectroscopy (EDS) that showed the presence of only Na, Cu, U, and S

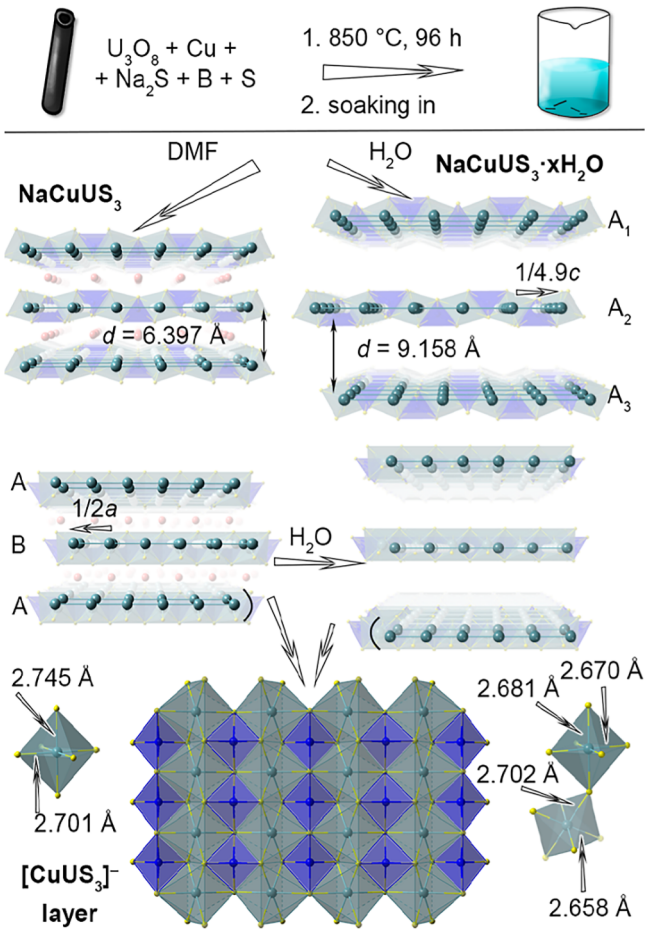

Figure 4. (top) Reaction scheme for obtaining $NaCuUS_3$ by dissolving the flux in anhydrous DMF and for obtaining $NaCuUS_3{\cdot}xH_2O$ via soaking in water. (middle) Comparison of interlayer distance and stacking arrangement between (left) $NaCuUS_3$ and (right) $NaCuUS_3{\cdot}xH_2O$. Dark green spheres represent U atoms. (bottom) $[CuUS_3]^-$ layers in both structures emphasizing difference in the US_6 polyhedra. Yellow spheres, blue tetrahedra, and gray octahedra represent S atoms, CuS_4 and US_6 polyhedra, respectively.

(Figures S4−S5 and Table S9) and confirmed that Na^+ ions remain within the crystal structure during water intercalation. The hydrated material is, therefore, best described by the formula $NaCuUS_3{\cdot}xH_2O$. Moreover, inductively coupled plasma optical emission spectroscopy (ICP-OES) showed that the concentration of Na, Cu, and U elements in single crystals of $NaCuUS_3{\cdot}xH_2O$ is in 1.06:0.99:1.00 ratio (Table S10), respectively, and in line with the proposed $NaCuUS_3{\cdot}xH_2O$ formula. PXRD patterns show the presence of only two crystalline phases, $NaCuUS_3$ and $NaCuUS_3{\cdot}xH_2O$ without any crystalline intermediates (Figure 5). Unlike previously reported $NaGaS_2$, which absorbs water from the atmosphere in minutes, $NaCuUS_3$ is stable in air for at least one day and hydration requires 4−5 days to reach completion, exhibiting significantly slower kinetics of hydration than $NaGaS_2$. This is the first example of SCSC hydration in layered actinides along with our previously demonstrated successful exfoliation of gallium sulfide sheets via sonication of the ion-exchanged $NaGaS_2{\cdot}H_2O$ in methanol or ethanol/water mixture,[77,78] suggesting that $NaCuUS_3{\cdot}xH_2O$ is a good candidate for creating new 2D actinide materials.

https://doi.org/10.1021/jacs.2c04783
J. Am. Chem. Soc. 2022, 144, 13773−13786

Table 2. Crystallographic Data for $ACuUQ_3{\cdot}xH_2O$ (s.g., $P2/m$, $Z = 2$)

compound	a, Å	b, Å	c, Å	β, °	R_1/wR_2, %
$NaCuUS_3{\cdot}xH_2O$	9.397(3)	3.9050(13)	10.235(3)	102.943 (14)	7.26/17.63
$KCuUS_3{\cdot}xH_2O$	8.9864(18)	3.9106(7)	10.1803(17)	100.340 (10)	11.61/27.23
$NaCuUSe_3{\cdot}xH_2O$	9.783(3)	4.0358(14)	10.571(3)	102.226 (13)	11.02/26.71

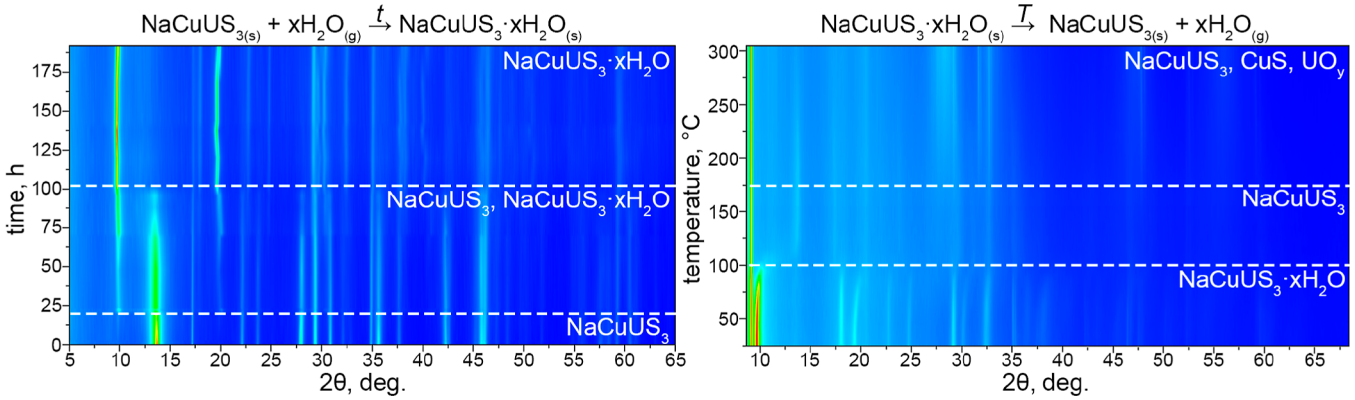

Figure 5. (left) Contour plot 2D image of the PXRD patterns for $NaCuUS_3$ in an ambient atmosphere over time. $NaCuUS_3$ in air starts converting to $NaCuUS_3{\cdot}xH_2O$ after 24 h. Transformation is almost complete after 100 h (right). Contour plot 2D image of the PXRD patterns for $NaCuUS_3{\cdot}xH_2O$ in the sealed borosilicate glass capillary as a function of temperature. After 100 °C, $NaCuUS_3{\cdot}xH_2O$ converts to the anhydrous phase. Upon further heating to 175 °C, the water vapor in the sealed capillary starts to react with the anhydrous material to form CuS and UO_y. The peak at ~9° is due to the borosilicate glass capillary.

To determine the water content, we performed thermogravimetric analysis (TGA) of $NaCuUS_3{\cdot}xH_2O$ powder and found mass losses of 5.9% in the 20−150 °C temperature range (Figure S26) which correspond to $x = 1.5$. According to PXRD of the post-TGA products, $NaCuUS_3{\cdot}xH_2O$ reverts to $NaCuUS_3$ (Figure S16), and hence the hydration of this 2D actinide chalcogenide is a reversible process. High-temperature PXRD (Figure 5) shows that $NaCuUS_3{\cdot}xH_2O$ fully converts to $NaCuUS_3$ after heating to 100 °C, which agreed well with TGA results.

The layer rearrangement in $NaCuUS_3$ upon the hydration/dehydration process is complex because of significant structure transformations that take place during water intercalation/deintercalation. Along with the increase in the interlayer distance, the stacking of the $[CuUS_3]^-$ layers changes upon hydration of $NaCuUS_3$ to $NaCuUS_3{\cdot}xH_2O$ (Figure 4). In anhydrous $NaCuUS_3$, the $[CuUS_3]^-$ layers are stacked in an AB sequence where the B layer is shifted by $a/2$ relative to the A layer. Upon hydration, due to the change in symmetry from orthorhombic to monoclinic, every other layer now shifts by $\sim c/4.86$ perpendicular to the a-direction of $NaCuUS_3$, resulting in an $A_1...A_n$ stacking pattern. The changes in stacking of 2D actinide layers is likely to result in stacking faults and an overall decrease in crystallinity, especially after several hydration−dehydration cycles. Interestingly, the U−S bonds slightly shorten, by around 0.03−0.04 Å (Table S4), upon hydration, a small but noticeable change that is in excess of the estimated standard deviation of <0.008 Å for U−S bonds. This shortening results in a slight increase in the BVS oxidation state of uranium from 3.84 in $NaCuUS_3$ to 4.25 and 4.31 in $NaCuUS_3{\cdot}xH_2O$. The BVS oxidation state of copper does not change and stays the same at 1.21−1.23. Overall, the hydration process has a major impact on layer stacking and interlayer distance but has little effect on the layers themselves, which indicates potential layer retention upon exfoliation of this material.

To confirm that the $[CuUS_3]^-$ layers remain intact upon hydration of the $NaCuUS_3$ and to locate the sodium cations, we performed extended X-ray absorption fine structure (EXAFS) studies on anhydrous, hydrated, and thermally dehydrated samples. Using X-ray absorption spectroscopy (XAS) data collected on the Cu K-edge and the U L_3-edge, followed by Fourier transformation of the EXAFS part of the data, we were able to analyze local geometries of Cu and U for $NaCuUS_3$, $NaCuUS_3{\cdot}xH_2O$, and $NaCuUS_3$_deh samples using the $NaCuUS_3$ crystal structure as a starting model (Figures S40−S45). All three samples exhibit tetrahedral and octahedral coordination for Cu and U sites, respectively. Cu−S and U−S bond lengths of all three samples remain unchanged within a standard deviation between samples (Figure 6 and Table S21). EXAFS data support the results of single crystal XRD and further confirm that the $[CuUS_3]^-$ layers stay intact during $NaCuUS_3$ hydration and even after $NaCuUS_3{\cdot}xH_2O$ dehydration. EXAFS can also be used to probe the Na position in $NaCuUS_3{\cdot}xH_2O$ through refinement of the U···Na interatomic distances. While there are two 4.2(2) Å and four 4.4(1) Å U···Na interatomic distances in the EXAFS fit $|\chi(R)|$ for the $NaCuUS_3$ sample, the $NaCuUS_3{\cdot}xH_2O$ sample refined to two 4.2(4) Å U···Na distances (see Supporting Information for more details). This fitted U···Na distance is closer to the 4.139(2) Å than the 4.512(2) Å distance found in the $NaCuUS_3$ crystal structure, indicating that Na^+ ions are still bound to one $[CuUS_3]^-$ layer via four Na−S bonds (see Supporting Information for more details, Figure S39). This result indicates that it is more likely to cleave two Na−S bonds than four during the hydration of the $NaCuUS_3$ structure. EXAFS analysis demonstrated $[CuUS_3]^-$ layer retention upon water intercalation/deintercalation as well as provided us with additional structural information concerning the Na position in the hydrated $NaCuUS_3{\cdot}xH_2O$ structure.

To identify other potential phases in the $ACuTQ_3$ family that can undergo this type of hydration process as well as to

https://doi.org/10.1021/jacs.2c04783
J. Am. Chem. Soc. 2022, 144, 13773−13786

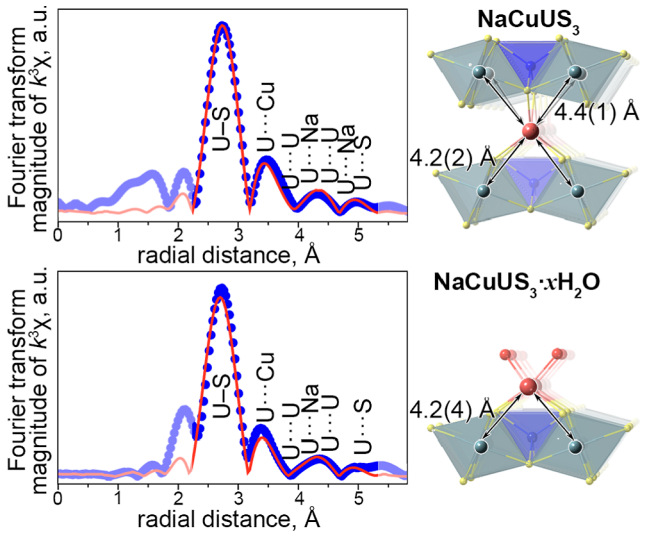

Figure 6. (Left) Phase-shifted Fourier transform magnitude of $k^3\chi$, $|\chi(R)|$, for (top) $NaCuUS_3$ and (bottom) $NaCuUS_3{\cdot}xH_2O$ samples. The bright color on $|\chi(R)|$ graph emphasizes the R-range used for EXAFS fitting. (Right) View of Na local structure for (top) $NaCuUS_3$ and (bottom) $NaCuUS_3{\cdot}xH_2O$ samples. Red, pink, yellow, and dark green spheres, blue tetrahedra, and gray octahedra represent O, Na, S, and U atoms, and CuS_4 and US_6 polyhedra, respectively. Arrows highlight U···Na distances refined from the EXAFS data.

garner additional insight into the process, we investigated the hydration of other $NaCuUS_3$ analogues, specifically, the K^+, Rb^+, and Cs^+ compositions. Interestingly, these compositions did not show any signs of hydration after soaking in water for several hours, indicating unfavorable hydration energetics/kinetics for the heavier alkali cation analogues (Figures S17, S22, and S24). However, prolonged soaking of $KCuUS_3$ (more than 12 h) leads to structural changes that are apparent in the PXRD pattern: a low intensity peak near 10° appears (Figure S18). IR spectroscopy (Figure S28) along with PXRD indicate that $KCuUS_3$ also undergoes hydration, albeit more slowly, further substantiated by the fact that it dehydrates and reverts to the original structure during annealing at 200 °C. We were able to isolate a single crystal of the hydrated potassium phase and to solve its crystal structure (see Supporting Information for more details), revealing that it is isostructural to $NaCuUS_3{\cdot}xH_2O$ (Figure S3). This result is in line with the higher solvation energies of Na^+ and K^+ cations, as corroborated with experimentally measured enthalpies of hydration for Na^+, K^+, Rb^+, and Cs^+, −409, −322, −293, and −264 kJ/mol, respectively.[77,79] Interestingly, prolonged soaking in water, that is, 24 h for $RbCuUS_3$ and $CsCuUS_3$ resulted in their decomposition (Figures S23 and S25 and Table S11). Moreover, we synthesized and tested a selenium-substituted phase, $NaCuUSe_3$, and found that it also undergoes hydration, resulting in the formation of $NaCuUSe_3{\cdot}xH_2O$ crystals that are isostructural to $NaCuUS_3{\cdot}xH_2O$ (Table 2). On the other hand, not all Na-containing compounds in the $AMTQ_3$ family undergo the hydration process. For example, the only other known Na-containing composition in the $KCuZrS_3$-structure type, $NaCuZrS_3$, does not undergo hydration when its crystals were separated from the flux by dissolving it in water (Figure S34),[59] indicating that the hydration either is unfavorable or kinetically hindered for this phase. Likewise, $NaCuNpS_3$ crystals were treated with water while dissolving the flux in which they were grown and resulted in a good diffraction data and a well refined crystal structure. Only the presence of some diffuse peaks in the diffraction data hint at the possible onset of a very slow hydration process or the presence of intrinsic stacking faults in the crystal (Figure S2). Therefore, the presence of Na^+ ions in a layered structure appears to be a necessary but not sufficient requirement for the hydration process (Figure S33, see Supporting Information for more details), highlighting an important role of other structural characteristics that can potentially be used to tune the hydration energetics as well as hydration kinetics in this family of materials.

Electronic Structure of $NaCuUS_3$, $NaCuUS_3{\cdot}xH_2O$, and $NaCuNpS_3$. 5f elements are fairly unique among the elements of the periodic table due to the existence of relativistic effects and the complex behavior of 5f electrons with respect to bonding to the surrounding atoms. To explore the contribution of the actinide element to the overall electronic structure, we calculated and analyzed the band structures and projected density of states (DOS) of the synthesized $NaCuUS_3$ and $NaCuNpS_3$, and the hypothesized $NaCuThS_3$ compounds (Figures 7 and S52). Substitution of Th^{4+} ($[Rh]5f^0$) to U^{4+}

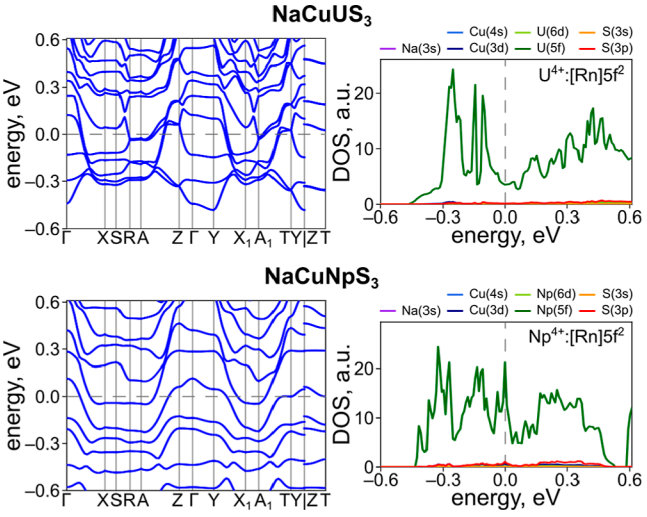

Figure 7. (Left) Spin−orbit coupled electronic structures and (right) projected DOS of (top) $NaCuUS_3$ and (bottom) $NaCuNpS_3$.

($[Rh]5f^2$) and Np^{4+} ($[Rh]5f^3$) drastically changes the electronic structure of these materials due to the valence electron configurations for the actinide element: from a non-magnetic semiconductor, $NaCuThS_3$, with a direct band gap of 1.95 eV to a magnetic $NaCuTS_3$ (T = U and Np) with metallic band structures (Figure 7 and Table S22). As a matter of fact, GGA potentials are known not to accurately predict experimental band gaps, and the band gaps discussed here are considered as a trend and not separately computed values. The $NaCuUS_3$ and $NaCuNpS_3$ band structures are potentially topologically non-trivial; however, additional calculations are needed to further evaluate this possibility. To understand the orbital contributions near the Fermi level, we plotted and analyzed the DOS of $NaCuUS_3$ and $NaCuNpS_3$ compounds (Figure 7), which shows that the partially occupied 5f orbitals have the largest contributions around the Fermi level. Very minor contributions from the 3d, 6d, and 3p orbitals of Cu, Np/U, and S, respectively, are also seen around the Fermi level due to the partial hybridization between the d and p orbitals within the CuS_4 and TS_6 (T = Np and U) polyhedra.

https://doi.org/10.1021/jacs.2c04783
J. Am. Chem. Soc. 2022, 144, 13773−13786

To estimate the band gaps of these materials, we performed UV−vis−NIR measurements on $ACuUS_3$ (A = Na, K, and Rb). The UV−vis−NIR spectra are dominated by sharp 5f−5f transitions at 0.53, 0.57, 0,67, 0.73, 0.91, and 0.95 eV (Figure 8) that are not affected by the A cation, corresponding to U^{4+}

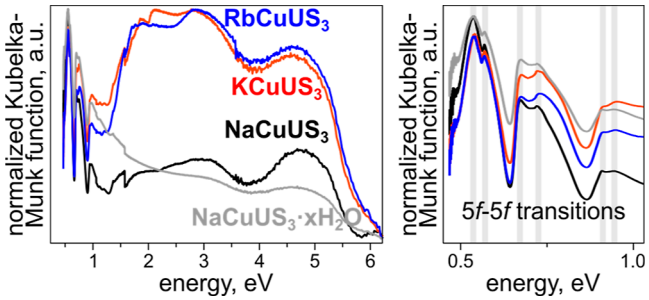

Figure 8. (Left) Normalized Kubelka−Munk function of $NaCuUS_3$ (black), $NaCuUS_3{\cdot}xH_2O$ (gray), $KCuUS_3$ (red), and $RbCuUS_3$ (blue) with (right) the highlight of 5f−5f transitions for U^{4+} ions.[80−83]

as observed for the reported U^{4+}-based materials.[80−83] There is no apparent band edge in the measured 0.47−6.2 eV range (Figure 8). This indicates that absorption edge is either masked by the 5f−5f transitions or that the band gap is less than 0.5 eV. Although band structure calculation combined with UV−vis−NIR spectroscopy supported metallic behavior of $NaCuUS_3$, we cannot for sure claim this and additional measurements are needed to be done in the future. To further compare the $NaCuUS_3$ and $NaCuNpS_3$ electronic structures, we estimated the Bader charge on Na, Cu, T (T = U and Np), and S elements (Table S23). While Bader charges for Na, Cu, and S are almost the same, the Bader charges on U, 1.93, and Np, 1.83, differ more significantly. In general, Bader charges are far from the nominal oxidation states of the elements and the deviation from the oxidation states indicates charge transfer from the atom to its surroundings. This result indicates that Np in $NaCuNpS_3$ participates in charge transfer, or covalent bonding, more effectively than U in $NaCuUS_3$. This is in line with the known trend that energy-degeneracy-driven covalency resulting from 5f orbitals increases as Th < U < Np < Pu.[84]

To understand how water incorporation affects the electronic structure of the material, we performed density functional theory (DFT) calculations of $NaCuUS_3{\cdot}xH_2O$. The $[CuUS_3]^-$ layers from the crystal structure of $NaCuUS_3{\cdot}xH_2O$ was used as a starting geometry model to which Na^+ ions were added to yield four Na−S bonds to the $[CuUS_3]^-$ layer as suggested by EXAFS fitting results. The remainder of the Na coordination environment was filled with water molecules, constrained so that the total number was 1.5 per formula unit (see Supporting Information for more details). After geometry optimization (Table S24), electronic structure calculations revealed that $NaCuUS_3{\cdot}xH_2O$ has a metallic band structure with a U 5f orbital contribution near the Fermi level (Figure S49). The UV−vis−NIR spectrum of $NaCuUS_3{\cdot}xH_2O$ was similar to the one collected for $NaCuUS_3$ with 5f−5f transitions corresponding to U^{4+} and no absorption edge in the 0.47−6.2 eV range (Figure 8). Comparison of Bader charges for U in $NaCuUS_3$ and $NaCuUS_3{\cdot}xH_2O$ revealed that after hydration, it remained at the same 1.93 value. Moreover, X-ray absorption near edge structure (XANES) spectroscopy confirmed that the oxidation states of Cu and U are invariant during hydration and dehydration, remaining at +1 and +4, respectively (Figures S36−S38 and Table S20; see Supporting Information for more details on XANES spectroscopy). To elaborate more on the electronic structure of these materials, we performed photoemission yield spectroscopy in air (PYSA) to determine the work function (WF) and valence band position with respect to vacuum. The analysis demonstrated that the WFs do not change significantly between $NaCuUS_3$ (WF = 5.0(6) eV) and $NaCuUS_3{\cdot}xH_2O$ (4.8(4) eV) samples (Figure S56). Moreover, the WFs are fairly constant among the $NaCuUS_3$ (WF = 5.0(6) eV), $KCuUS_3$ (WF = 5.2(2) eV), and $RbCuUS_3$ (WF = 5.3(3) eV) samples as well (Figure S56). This result is consistent with DFT calculations that demonstrated no significant contribution of the A metal's ns orbital to the valence or conductance bands for $ACuThS_3$ (A = Na, K, Rb, and Cs) and $NaCuTS_3$ (T = U and Np) materials (Figures 7 and S50−S55; see Supporting Information for more details). Overall, electronic structure calculations, XANES spectroscopy, and UV−vis near IR and WF measurements show that the changes to the interlayer distance via A metal or water incorporation do not drastically impact the electronic properties of $ACuUS_3$ (A = Na, K, and Rb) or $NaCuUS_3{\cdot}xH_2O$ and thus demonstrate that they are primarily dependent on the $[CuTS_3]^-$ layers.

CONCLUSIONS

In summary, we demonstrated the synthesis of new transuranium compound guided by DFT energetic calculations and crystal chemical reasoning and performed the first successful synthesis of a transuranium sulfide, $NaCuNpS_3$, using the BCM method. Previously, all known neptunium sulfide crystal structures were obtained from reactions involving Np metal. In the case of the BCM synthesis of $NaCuNpS_3$, the starting material, NpO_2, was heated with boron and sulfur and other reagents for an in situ formation of Np sulfide, which participated in the crystal growth reaction of $NaCuNpS_3$. Moreover, the BCM method was further extended to flux crystal growth of actinide selenides, through synthesis of the uranium analogue, $NaCuUSe_3$. In the future, the implementation of the BCM method will simplify the process of transuranium chalcogenides synthesis due to the ability to use all oxygen stable starting materials. This will benefit crystal chemistry of transuranium chalcogenides as well as fundamental studies of 5f electrons behavior in a soft ligand environment.

The reversible hydration in $NaCuUS_3$ single crystals was discovered and, while single crystals of $NaCuNpS_3$ are not as sensitive to water, the isostructural layered $NaCuUS_3$ phase exhibits interlayer water absorption, with a corresponding significant volume expansion and slight layer rearrangement. SCXRD, PXRD, high temperature PXRD, EXAFS and IR spectroscopies, and TGA studies were performed to derive the $NaCuUS_3{\cdot}xH_2O$ ($x \approx 1.5$) formula, and they support that the local structure within the layers remains unchanged throughout the hydration−dehydration process. In addition to that, we targeted a family of uranium-based analogues, $ACuUS_3$ (A = Na, K, Rb, and Cs), in which the $NaCuUS_3$ and $KCuUS_3$ compositions undergo SCSC hydration forming $NaCuUS_3{\cdot}xH_2O$ and $KCuUS_3{\cdot}xH_2O$. Thus, the incorporation of water molecules between the layers is driven by significant negative hydration enthalpy of Na^+ and K^+ ions. Na^+ ion hydration was not observed in $NaCuNpS_3$, which shows that not only spacer ion control water uptake but also slight changes in the layers

https://doi.org/10.1021/jacs.2c04783
J. Am. Chem. Soc. 2022, 144, 13773−13786

structure can significantly affect the energetics/kinetics of the hydration process. Overall, water uptake in layered actinide chalcogenides offers a unique opportunity to study physical properties, for instance, magnetism, of 5f electron confined in 2D materials.

Band structure calculations of $NaCuUS_3$ and $NaCuNpS_3$ showed that these materials are metals with the domination of 5f electrons near the Fermi level. UV−vis−NIR measurements demonstrated that the $NaCuUS_3$ sample absorbs photons down to 0.47 eV, implying that both $NaCuUS_3$ and $NaCuNpS_3$ materials are either narrow band gap semiconductors or metals. In addition, XANES, UV−vis−NIR, and WF measurements on $ACuUS_3$ (A = Na, K, and Rb) and $NaCuUS_3{\cdot}xH_2O$ samples, as well as electronic structure calculation of $NaCuUS_3$, $NaCuUS_3{\cdot}xH_2O$, and $NaCuNpS_3$ materials demonstrated that electronic properties arise from the $[CuTS_3]^-$ layers and show little dependence in the interlayer separation. Along with the previous calculations on K-, Rb-, and Cs-containing analogues,[58] which indicates potential non-trivial topological behavior in this structure family, $NaCuUS_3$ and $NaCuNpS_3$ band structures are potentially topologically non-trivial; however, additional calculations are needed to further evaluate this possibility.

EXPERIMENTAL SECTION

Caution! Both thorium and uranium are radioactive. Although the uranium precursor used in this synthesis contains depleted uranium, proper procedures for handling radioactive materials must be observed. All handling of radioactive materials was performed in laboratories specially designated for the study of radioactive actinide materials. Serious health risks are associated with handling neptunium since is ^{237}Np is an α - and γ-emitter. Proper precautions must be taken. All studies were conducted in a laboratory designated for transuranics research.

Materials. The following materials were used as received without further purification: B (CERAC, 99.5%), S (Fisher Scientific, 99%), Cu (Johnson Matthey, 99.9%), Se (Alfa Aesar, 99.999%), Na_2CO_3 (Fisher Scientific, 99%), K_2CO_3 (BDH, 99.0%), Rb_2CO_3 (Alfa Aesar, 99%), Cs_2CO_3 (BTC, 99.9%), ThO_2 (Strem Chemicals, 99.99%), U_3O_8 (MV Laboratories, 99.9%), dimethylformamide (DMF, Sigma-Aldrich, 99.8%), and acetone (BDH, 99.5%). Synthesis of Na_2S and K_2S was performed using a reported procedure.[85] U_3O_8 was annealed at 800 °C for 24 h before use and stored at 260 °C in a drying oven. A_2CO_3 (A = K, Rb, and Cs) was stored at 260 °C in the drying oven. For all mentioned reactions, masses of the reagents listed in Table S1 were mixed inside a carbon crucible which was placed inside a silica tube. Typically, the silica tube was flame-sealed under a vacuum of $<10^{-4}$ Torr and placed in a metal spring for containment should the tube bursts due to carbon dioxide pressure build up. The sealed tube inside the metal spring was placed vertically into a programmable box furnace with the corresponding temperature profile listed in Table S1. Once at room temperature, the tube was cut open and the carbon crucible containing the reaction products was placed into a beaker filled with respective solvent. All mentioned single crystals except neptunium were analyzed by EDS spectroscopy to confirm elemental composition (Table S9 and Figures S4−S10).

Synthesis of Single Crystals. *$NaCuUQ_3$ and $NaCuUQ_3{\cdot}xH_2O$.* The starting reagents, U_3O_8, Cu, Na_2CO_3, B, and Q (Q = S or Se), were used to grow the single crystal of $NaCuUQ_3$. After the reaction was complete, the product was soaked in DMF for several hours and the crystals were isolated by filtration, washed with acetone, and allowed to air dry. $NaCuUQ_3{\cdot}xH_2O$ (Q = S and Se) crystals were obtained after soaking the resulting product in a DMF/water mixture. A sample of $NaCuUQ_3$ (Q = S and Se) was contaminated with $Na_2B_8O_{13}$ as indicated by additional peaks in the PXRD pattern (Figures S11 and S12).

$NaCuNpS_3$. All experiments with Np samples were carried out in Department of Chemistry and Biochemistry, Radiochemistry Program, University of Nevada. 0.0060 g of neptunium oxide (NpO_2) was pressed into a pellet without grinding in the glovebox along with other reagents, Cu (0.0085 g), Na_2CO_3 (0.0126 g), B (0.0116 g), and S (0.0515 g), resulting in a 3:18:16:144:216 molar ratio. After reaction was complete, the product was soaked in water overnight and crystals were picked from the solution.

$ACuThS_3$. The starting reagents, ThO_2, Cu, A_2CO_3 (A = K, Rb, or Cs), B, and S, were used to grow single crystal of $ACuUS_3$. After the reaction was complete, the product was soaked in water overnight and crystals were isolated by filtration.

X-ray Crystal Structure Determination. *$NaCuUS_3$, $NaCuUSe_3$, $NaCuNpS_3$, $KCuThS_3$, $RbCuThS_3$, and $CsCuThS_3$.* The compounds crystallize in the orthorhombic crystal system, space group *Cmcm*. The asymmetric unit consists of one alkali atom, one Cu atom, one actinide atom, and two chalcogen atoms. The largest residual electron density peak in the final difference map is 1.29/1.86/4.61/2.41/0.92/1.33 e−/Å^3, located 0.78/1.66/0.95/0.83/0.75/0.91 Å from Na1/Se1/Np1/Th1/Th1/Th1, respectively. The crystallographic data and results of the diffraction experiments are summarized in Tables S2−S7.

$NaCuUS_3{\cdot}xH_2O$, $KCuUS_3{\cdot}xH_2O$, and $NaCuUSe_3{\cdot}xH_2O$. The compounds crystallize in the monoclinic crystal system, space group *P2/m*. The asymmetric unit consists of one Cu atom, two U atoms, and three S/S/Se atoms, respectively. For the $NaCuUS_3{\cdot}xH_2O$ structure, the Cu atom position was split into two crystallographic sites, and the occupancy of the Cu sites was refined, which resulted in occupancies of 78.3 and 21.7%. Due to the low quality of the crystals, only the $[CuUQ_3]^-$ (Q = S and Se) layers in the structure of $NaCuUQ_3{\cdot}xH_2O$ were determined. The structures contain large spaces between $[CuUQ_3]^-$ (Q = S and Se) sheets, presumably filled with heavily disordered water molecules and Na/K/Na ions, which could not be clearly identified or modeled. The content in these spaces was modeled with Squeeze in PLATON.[86] The solvent-accessible volume of 74/67/76 Å^3 was calculated, containing the equivalent of 43/9/62 electrons per formula unit, respectively.

For $NaCuUS_3{\cdot}xH_2O$ and $NaCuUSe_3{\cdot}xH_2O$, the scattering contribution of this electron density was added to the structure factors computed from the modeled part of the structure during refinement. The reported crystal density and F.W. are calculated from the known part of the structure only. The largest residual electron density peak in the final difference map is 7.03/14.54 e$^-$/Å^3, located 0.95/1.09 Å from U1/U1, respectively. The crystallographic data and results of the diffraction experiments are summarized in Tables S2, S4, and S6.

In addition, for $KCuUS_3{\cdot}xH_2O$, we modeled the positions of K and O between $[CuUS_3]^-$ layers as the highest Q-peaks between the layers (at least 3 Å distant from the $[CuUS_3]^-$ sheets). The asymmetric unit consists of one Cu atom, two U atoms, three S atoms, two K atoms with 1/2 occupancy, and two O atoms with 1/2 occupancy, respectively. Due to the low quality of the crystals that were decomposing during data collection, there are numerous residual electron density peaks, mostly located near the U atom and the $[CuUS_3]^-$ sheets. While collecting SCXRD and analyzing the degree of hydration of $KCuUS_3$ via PXRD, we noticed that $KCuUS_3$ or $KCuUS_3{\cdot}xH_2O$ rapidly converts to $K_2(UO_2)_6O_4(OH)_6{\cdot}7H_2O$ (mineral compreignacite). To illustrate, a fast scan initially yielded an $R_1[I \geq 2\sigma(I)]$ as 0.0937, while a complete scan executed subsequently using the same crystal over a couple of hours had an $R_1[I \geq 2\sigma(I)]$ = 0.1161. Furthermore, after 2 days, a unit cell check of the same crystal yielded a different unit cell. Forcing the lattice parameters of this crystal to the previous $KCuUS_3{\cdot}xH_2O$ unit cell, the resulted $R_1[I \geq 2\sigma(I)]$ turned to 0.7869. The increase of $R_1[I \geq 2\sigma(I)]$ over time suggests that $KCuUS_3{\cdot}xH_2O$ is not stable in air and may quickly decompose. K and O positions in the $KCuUS_3{\cdot}xH_2O$ structure were not apparent from the residual electron density peaks; nonetheless, the suggested model has reasonable K−S bond lengths as well as K coordination and is relevant for comparison with the $KCuUS_3$ structure (additional details can be found in the structure description

https://doi.org/10.1021/jacs.2c04783
J. Am. Chem. Soc. 2022, 144, 13773−13786

section in the SI). The crystallographic data and results of the diffraction experiments are summarized in Tables S2, S4, and S6.

X-ray Absorption Spectroscopy. Cu K-edge and U L_3-edge XANES and EXAFS experiments were carried out at beamline 10ID-B, operated by the Materials Research Collaborative Access Team (MRCAT) at the Advanced Photon Source (APS), Argonne National Laboratory (ANL). Data reduction, data analysis, and EXAFS fitting were performed with the Athena, Artemis, and IFEFFIT software packages.[87] Approximately 11 mg of sample was diluted with 32 mg of BN, well ground, and packed into a nylon washer with inner diameter of 0.71 cm and thickness of 0.08 cm. The nylon washer was sealed on both sides using 0.06 mm-thickness Kapton tape as the primary containment. Then the sealed washer was heat-sealed inside a polypropylene heat-sealed bag. One more layer of Kapton tape was added for secondary containment. The Cu K-edge and U L_3-edge spectra were recorded in both transmission and fluorescence mode at room temperature. For energy calibration, copper (E_0 = 8979 eV) and zirconium (E_0 = 17998 eV) foil spectra were measured simultaneously while measuring Cu K-edge and U L_3-edge spectra, respectively. Transmission data were measured from 8700 to 9900 eV with a step size of 0.45 eV for the Cu region and from 16,795 to 18,190 eV with a step size of 0.8 eV for the U EXAFS region. The acquisition time was approximately 13.5 and 3.5 min for the Cu K-edge and U L_3-edge spectra with total number of 15 and 6 scans, respectively.

Computational Details. All DFT calculations were carried out using the Vienna Ab initio Simulation Package (VASP)[88,89] utilizing the projector augmented-wave (PAW) potential.[90] The PBE parametrization of the generalized gradient approximation (GGA) to the exchange−correlation functional was used for the calculations.[91] We used the following potentials of the constituent elements: H ($1s^1$), O ($2s^2$, $2p^4$), Na_pv ($2p^6$ $3s^1$), S ($3s^2$ $3p^4$), K_sv ($3s^2$ $3p^6$ $4s^1$), Cu ($3d^{10}$ $4s^1$), Se ($4s^2$ $4p^4$), Rb_sv ($4s^2$ $4p^6$ $5s^1$), Te ($5s^2$ $5p^4$), Th ($5f^0$ $6s^2$ $6p^6$ $6d^2$ $7s^2$), U ($5f^3$ $6s^2$ $6p^6$ $6d^1$ $7s^2$), and Np ($5f^4$ $6s^2$ $6p^6$ $6d^1$ $7s^2$). All compounds were structurally relaxed (volume, cell shape, and atomic positions), starting from their experimentally known crystal structures, where available, following the DFT settings in the OQMD.[69,70] The threshold for energy and force convergence were set to 10^{-8} eV and 10^{-3} eV/Å, respectively. The relaxed geometries of the $ACuTQ_3$ compounds preserve the *Cmcm* space group during structure relaxation. For geometry relaxation of $NaCuUS_3$, the·$1.5H_2O$ *P*1 space group was used. The energy cutoff for the DFT calculations was set to 520 eV for static calculations. The optimized lattice constants agree very well (error < 2.6%) with the experimental values (Table S22). We calculated the electronic structures of the compounds following the *k*-point convention given by Setyawan and Curtarolo.[92] Spin−orbit coupling (SOC) was included during the calculations of the electronic structures. We calculated the Bader charges of the atoms in $NaCuUS_3$, $NaCuNpS_3$, and $NaCuUS_3{\cdot}xH_2O$ using the Bader Charge Analysis tool[93,94] by manipulating the charge density produced with VASP. The charge density used for Bader analysis combines the valence and core charge densities.

The $ACuTS_3$ compounds, although layered, are not typical van der Waals (vdW) materials. In the crystal structures of these compounds, rows of A^+ cations stack alternatively with the $[CuTS_3]^-$ anionic layers formed. Due to the charges on the layers, they interact through electrostatic rather than the vdW interactions. However, to check the effect of vdW interactions, we optimized the crystal structures of the non-hydrated compounds in Table 1 with the inclusion of vdW interactions utilizing the DFT-D2 method of Grimme.[95] The optimized lattice constants are given in Table S22. We notice that vdW interactions only marginally improve the lattice constants for the Th-containing compounds; however, the lattice constants for the U- and Np containing compounds are worse compared to lattice constants obtained with calculations that do not include vdW interactions. Since the error in the optimized lattice constants obtained without the inclusion of the vdW interactions are within the typical error of DFT calculations, it indicates that conventional DFT calculations captures the crystal geometries well.

The participation of 5f-electrons in chemical bonding is generally not well understood in actinides. Recently, Vitova and co-workers revealed the role of 5f valence orbitals in covalent bonding in early actinide oxides.[96] In relation to the current work, we investigated the bonding environment of $NaCuUS_3$ using DFT calculations. To analyze the chemical bonding in $NaCuUS_3$, we plotted the iso-surface (at an iso-value of 0.05 e/bohr^3) of charge densities (Figure S46), which reveals the strong overlapping charge clouds between the U and S atoms, indicating covalent bonding interactions between them. Thus, our calculations present evidence that the 5f-electrons of the actinide elements participate in covalent bonding with the chalcogen atoms in the $NaCuTS_3$ family of compounds and therefore stay weakly localized, which helps to stabilize the compounds.

It is worth noting that semilocal exchange−correlation functional such as the GGA is well known to underestimate the band gaps of compounds. Hence, to calculate the electronic structures and the band gaps more accurately within DFT, advanced exchange−correlation functionals such as meta GGA, hybrid functionals,[97] or many-body perturbation theory (e.g., GW method) might be necessary. Nonetheless, one of the drawbacks of conventional DFT is the prediction of metallic band structures for correlated insulators (such as the Mott insulator) due to the erroneous over delocalization of the valence bands consisting of d or f-electrons around the Fermi level. The introduction of a Hubbard *U* term to the DFT Hamiltonian localize these orbitals, opening a gap around the Fermi level.[98] To check the effect of the Hubbard *U* parameter on the properties of the quaternary actinides, we applied the DFT + *U* method to $NaCuUS_3$. There is no unique way of choosing the *U* parameter for an element in a compound. Usually, the value of the Hubbard *U* parameter is varied until good agreement is achieved between the calculated and experimental measured properties (such as the band gap, lattice constants, etc.). It was shown by Pegg and co-workers[99] that for the actinide elements in binary oxides, choosing the *U*-parameter between 3−7 eV give rise to good agreement between the calculated and experimental results. In the presented study, we took different values of the *U* parameter, namely, *U* = 1, 2, 4, and 6 eV and fully optimized the crystal structures of $NaCuUS_3$ to check the agreement between the calculated and experimental lattice constants. We found that the DFT + *U* optimized lattice constants are not better than the conventional DFT simulated lattice constants (Table S22) in comparison with the experiential values. The calculated band gaps with different *U* parameters also vary quite strongly (Figure S47). Our experiments (UV−vis−NIR measurements) on $ACuUS_3$ (*A* = Na, K, and Rb) did not reveal the presence of a band edge (and hence the absence of a band gap) in these compounds, possibly because the band edge is masked by the 5f−5f transition or the presence of small band gap (<0.5 eV), which is beyond the current experimental resolution. As 5f orbitals of U in $NaCuUS_3$ are involved in covalent bonding with the chalcogen atoms, they stay weakly localized. Since the lattice constants of $NaCuUS_3$ optimized using the DFT + *U* method are worse than those obtained without the *U* parameter and the band gap varies strongly as a function of the *U* values (Table S22 and Figure S47), it seems plausible that the DFT + *U* method does not describe the crystal geometry and electronic structure of this compound well.

■ ASSOCIATED CONTENT

Supporting Information

The Supporting Information is available free of charge at https://pubs.acs.org/doi/10.1021/jacs.2c04783.

Crystallographic tables, BVS table, structure figures, PXRD patterns, EDS, IR, XANES, EXAFS, and PYSA spectra, TGA plot, and band structure figures (PDF)

Accession Codes

CCDC 2155983−2155991 contain the supplementary crystallographic data for this paper. These data can be obtained free of charge via www.ccdc.cam.ac.uk/data_request/cif, or by emailing data_request@ccdc.cam.ac.uk, or by contacting The

https://doi.org/10.1021/jacs.2c04783
J. Am. Chem. Soc. 2022, 144, 13773−13786

Cambridge Crystallographic Data Centre, 12 Union Road, Cambridge CB2 1EZ, UK; fax: +44 1223 336033.

AUTHOR INFORMATION

Corresponding Author

Hans-Conrad zur Loye − *Department of Chemistry and Biochemistry, University of South Carolina, Columbia, South Carolina 29208, United States;* orcid.org/0000-0001-7351-9098; Email: zurloye@mailbox.sc.edu

Authors

Anna A. Berseneva − *Department of Chemistry and Biochemistry, University of South Carolina, Columbia, South Carolina 29208, United States*

Vladislav V. Klepov − *Department of Chemistry and Biochemistry, University of South Carolina, Columbia, South Carolina 29208, United States; Department of Chemistry, Northwestern University, Evanston, Illinois 60208, United States;* orcid.org/0000-0002-2039-2457

Koushik Pal − *Department of Materials Science and Engineering, Northwestern University, Evanston, Illinois 60208, United States;* orcid.org/0000-0002-5426-9748

Kelly Seeley − *Department of Chemistry and Biochemistry, Radiochemistry Program, University of Nevada, Las Vegas, Nevada 89154, United States*

Daniel Koury − *Department of Chemistry and Biochemistry, Radiochemistry Program, University of Nevada, Las Vegas, Nevada 89154, United States*

Joseph Schaeperkoetter − *Kazuo Inamori School of Engineering, Alfred University, Alfred, New York 14802, United States*

Joshua T. Wright − *Illinois Institute of Technology, Chicago, Illinois 60616, United States*

Scott T. Misture − *Kazuo Inamori School of Engineering, Alfred University, Alfred, New York 14802, United States;* orcid.org/0000-0003-1604-8044

Mercouri G. Kanatzidis − *Department of Chemistry, Northwestern University, Evanston, Illinois 60208, United States;* orcid.org/0000-0003-2037-4168

Chris Wolverton − *Department of Materials Science and Engineering, Northwestern University, Evanston, Illinois 60208, United States;* orcid.org/0000-0003-2248-474X

Artem V. Gelis − *Department of Chemistry and Biochemistry, Radiochemistry Program, University of Nevada, Las Vegas, Nevada 89154, United States;* orcid.org/0000-0002-5487-1472

Complete contact information is available at: https://pubs.acs.org/10.1021/jacs.2c04783

Author Contributions

The manuscript was written through contributions of all authors. All authors have given approval to the final version of the manuscript.

Notes

The authors declare no competing financial interest.

ACKNOWLEDGMENTS

This research was supported by the US Department of Energy, Office of Basic Energy Sciences, Division of Materials Sciences and Engineering under award DE-SC0018739. Specifically, DE-SC0018739 supported all sample synthesis and structure determinations, sample characterization, data collection at MRCAT, and data analysis. MRCAT operations are supported by the Department of Energy and the MRCAT member institutions. This research used resources of the Advanced Photon Source, a U.S. Department of Energy Office of Science User Facility operated for the DOE Office of Science by Argonne National Laboratory under contract no. DE-AC02-06CH11357. K.P. and C.W. acknowledge funding support from the National Institute of Standards and Technology as part of the Center for Hierarchical Materials Design (CHiMaD) under the Award 70NANB19H005 by U.S. Department of Commerce which supported DFT calculations. V.V.K. and M.G.K. acknowledge the National Science Foundation Grant DMR-2003476 for UV−vis−NIR measurements and PYSA spectroscopy. We thank Mina Aziziha and Juliano Schorne-Pinto for their assistance in ICP-OES measurements. We are also grateful for assistance with radioactive material transportation by radiation safety officers of the University of South Carolina, Argonne National Laboratory, and Northwestern University.

REFERENCES

(1) Méot-Reymond, S.; Fournier, J. M. Localization of 5f electrons in δ-plutonium: Evidence for the Kondo effect. *J. Alloys Compd.* **1996**, *232*, 119−125.

(2) Söderlind, P.; Sadigh, B.; Lordi, V.; Landa, A.; Turchi, P. E. A. Electron correlation and relativity of the 5f electrons in the U−Zr alloy system. *J. Nucl. Mater.* **2014**, *444*, 356−358.

(3) Joyce, J. J.; Wills, J. M.; Durakiewicz, T.; Butterfield, M. T.; Guziewicz, E.; Moore, D. P.; Sarrao, J. L.; Morales, L. A.; Arko, A. J.; Eriksson, O.; Delin, A.; Graham, K. S. Dual nature of the 5f electrons in plutonium materials. *Physica B* **2006**, *378*−*380*, 920−924.

(4) Morss, L. R.; Edelstein, N. M.; Fuger, J.; Katz, J. J.; Morss, L. R. *The Chemistry of the Actinide and Transactinide Elements*; Springer: Dordrecht, 2006.

(5) Bauer, E. D.; Altarawneh, M. M.; Tobash, P. H.; Gofryk, K.; Ayala-Valenzuela, O. E.; Mitchell, J. N.; McDonald, R. D.; Mielke, C. H.; Ronning, F.; Griveau, J. C.; Colineau, E.; Eloirdi, R.; Caciuffo, R.; Scott, B. L.; Janka, O.; Kauzlarich, S. M.; Thompson, J. D. Localized 5f electrons in superconducting $PuCoIn_5$: consequences for superconductivity in $PuCoGa_5$. *J. Phys.: Condens. Matter* **2012**, *24*, 052206.

(6) Mesbah, A.; Prakash, J.; Ibers, J. A. Overview of the crystal chemistry of the actinide chalcogenides: incorporation of the alkaline-earth elements. *Dalton Trans.* **2016**, *45*, 16067−16080.

(7) Castro, L.; Yahia, A.; Maron, L. Are 5f Electrons Really Active in Organoactinide Reactivity? Some Insights from DFT Studies. *ChemPhysChem* **2010**, *11*, 990−994.

(8) Zwicknagl, G.; Fulde, P. The dual nature of 5f electrons and the origin of heavy fermions in U compounds. *J. Phys.: Condens. Matter* **2003**, *15*, S1911.

(9) Diamond, R. M.; Street, K., Jr; Seaborg, G. T. An ion-exchange study of possible hybridized 5f bonding in the actinides. *J. Am. Chem. Soc.* **1954**, *76*, 1461−1469.

(10) Takahashi, T.; Sato, N.; Yokoya, T.; Chainani, A.; Morimoto, T.; Komatsubara, T. Dual character of 5f electrons in UPd_2Al_3 observed by high-resolution photoemission spectroscopy. *J. Phys. Soc. Jpn.* **1996**, *65*, 156−159.

(11) Serezhkin, V. N.; Verevkin, A. G.; Pushkin, D. V.; Serezhkina, L. B. Maximum filling principle and sublattices of actinide atoms in crystal structures. *Russ. J. Coord. Chem.* **2008**, *34*, 225−232.

(12) Dufaye, M.; Duval, S.; Loiseau, T. Trends and new directions in the crystal chemistry of actinide oxo-clusters incorporated in polyoxometalates. *CrystEngComm* **2020**, *22*, 3549−3562.

(13) Benedict, U.; Peterson, J. R.; Haire, R. G.; Dufour, C. Delocalisation of 5f electrons in berkelium and californium metals under pressure. *J. Phys. F: Met. Phys.* **1984**, *14*, L43.

(14) Veal, B. W.; Lam, D. J. Bonding in uranium oxides: The role of 5f electrons. *Phys. Lett. A* **1974**, *49*, 466−468.

(15) Smith, P. A.; Hickam, S. M.; Szymanowski, J. E. S.; Burns, P. C. Mixed-Valent Cyanoplatinates Featuring Neptunyl-Neptunyl Cation-Cation Interactions. *Inorg. Chem.* **2018**, *57*, 9504−9514.
(16) Almond, P. M.; Skanthakumar, S.; Soderholm, L.; Burns, P. C. Cation−Cation Interactions and Antiferromagnetism in $Na[Np(V)O_2OH)_2]$: Synthesis, Structure, and Magnetic Properties. *Chem. Mater.* **2007**, *19*, 280−285.
(17) Forbes, T. Z.; Burns, P. C.; Skanthakumar, S.; Soderholm, L. Synthesis, structure, and magnetism of Np_2O_5. *J. Am. Chem. Soc.* **2007**, *129*, 2760−2761.
(18) Polinski, M. J.; Garner, E. B.; Maurice, R.; Planas, N.; Stritzinger, J. T.; Parker, T. G.; Cross, J. N.; Green, T. D.; Alekseev, E. V.; Van Cleve, S. M.; Depmeier, W.; Gagliardi, L.; Shatruk, M.; Knappenberger, K. L.; Liu, G.; Skanthakumar, S.; Soderholm, L.; Dixon, D. A.; Albrecht-Schmitt, T. E. Unusual structure, bonding and properties in a californium borate. *Nat. Chem.* **2014**, *6*, 387−392.
(19) Polinski, M. J.; Grant, D. J.; Wang, S.; Alekseev, E. V.; Cross, J. N.; Villa, E. M.; Depmeier, W.; Gagliardi, L.; Albrecht-Schmitt, T. E. Differentiating between trivalent lanthanides and actinides. *J. Am. Chem. Soc.* **2012**, *134*, 10682−10692.
(20) Murphy, G. L.; Wang, Y.; Kegler, P.; Wang, Y.; Wang, S.; Alekseev, E. V. The first actinide polyiodate: a complex multifunctional compound with promising X-ray luminescence properties and proton conductivity. *Chem. Commun.* **2021**, *57*, 496−499.
(21) Colliard, I.; Morrison, G.; Loye, H. Z.; Nyman, M. Supramolecular Assembly of U(IV) Clusters and Superatoms with Unconventional Countercations. *J. Am. Chem. Soc.* **2020**, *142*, 9039−9047.
(22) Gil, A.; Karhánek, D.; Miró, P.; Antonio, M. R.; Nyman, M.; Bo, C. A journey inside the U_{28} nanocapsule. *Chem.—Eur. J.* **2012**, *18*, 8340−8346.
(23) Griveau, J.-C.; Colineau, É. Superconductivity in transuranium elements and compounds. *C. R. Phys.* **2014**, *15*, 599−615.
(24) Hill, H. H. Superconductivity in the "actinide" elements. *Physica* **1971**, *55*, 186−206.
(25) Brodsky, M. B. Magnetic properties of the actinide elements and their metallic compounds. *Rep. Prog. Phys.* **1978**, *41*, 1547.
(26) Santini, P.; Lémanski, R.; Erdős, P. Magnetism of actinide compounds. *Adv. Phys.* **1999**, *48*, 537−653.
(27) Sundar, S.; Gheidi, S.; Akintola, K.; Côté, A. M.; Dunsiger, S. R.; Ran, S.; Butch, N. P.; Saha, S. R.; Paglione, J.; Sonier, J. E. Coexistence of ferromagnetic fluctuations and superconductivity in the actinide superconductor UTe_2. *Phys. Rev. B* **2019**, *100*, 140502.
(28) Ott, H. R.; Rudigier, H.; Fisk, Z.; Smith, J. L. UBe_{13}: An Unconventional Actinide Superconductor. *Phys. Rev. Lett.* **1983**, *50*, 1595−1598.
(29) zur Loye, H.-C.; Besmann, T.; Amoroso, J.; Brinkman, K.; Grandjean, A.; Henager, C. H.; Hu, S.; Misture, S. T.; Phillpot, S. R.; Shustova, N. B.; Wang, H.; Koch, R. J.; Morrison, G.; Dolgopolova, E. Hierarchical Materials as Tailored Nuclear Waste Forms: A Perspective. *Chem. Mater.* **2018**, *30*, 4475−4488.
(30) Chemey, A. T.; Celis-Barros, C.; Huang, K.; Sperling, J. M.; Windorff, C. J.; Baumbach, R. E.; Graf, D. E.; Páez-Hernández, D.; Ruf, M.; Hobart, D. E.; Albrecht-Schmitt, T. E. Electronic, Magnetic, and Theoretical Characterization of $(NH_4)_4UF_8$, a Simple Molecular Uranium(IV) Fluoride. *Inorg. Chem.* **2019**, *58*, 637−647.
(31) Chandrasekar, A.; Ghanty, T. K. Uncovering Heavy Actinide Covalency: Implications for Minor Actinide Partitioning. *Inorg. Chem.* **2019**, *58*, 3744−3753.
(32) Pace, K. A.; Klepov, V. V.; Berseneva, A. A.; Loye, H. Covalency in Actinide Compounds. *Chem.—Eur. J.* **2021**, *27*, 5835−5841.
(33) Gmelin, L. *Transurane (Erganszungswerk)*; ACS Publications, 1972.
(34) Damien, D.; Damien, N.; Jove, J.; Charvillat, J. P. Some neptunium selenides. *Inorg. Nucl. Chem. Lett.* **1973**, *9*, 649−655.
(35) Bugaris, D. E.; Ibers, J. A. Syntheses and characterization of some solid-state actinide (Th, U, Np) compounds. *Dalton Trans.* **2010**, *39*, 5949.
(36) Hellenbrandt, M. The Inorganic Crystal Structure Database (ICSD)—Present and Future. *Crystallogr. Rev.* **2004**, *10*, 17−22.
(37) Damien, D. Synthèse et Cristallochimie des Chalcogénures de Transuraniens: Contribution à l'Étude de la Localisation des Électrons 5f. Doctoral Dissertation, 1976.
(38) Thevenin, T.; Damien, D. *Transuranium Element Chalcogenides. Crystallochemistry and Moessbauer Spectrometry of Neptunium 237 Chalcogenides*. No. CEA-CONF--5904; CEA Centre d'Etudes Nucleaires de Fontenay-aux-Roses, 1981.
(39) Wells, D. M.; Chan, G. H.; Ellis, D. E.; Ibers, J. A. $UTa_2O(S_2)_3Cl_6$: A ribbon structure containing a heterobimetallic 5d−5f M_3 cluster. *J. Solid State Chem.* **2010**, *183*, 285−290.
(40) Mesbah, A.; Ibers, J. A. Syntheses and crystal structures of three barium uranium sulfides. *J. Solid State Chem.* **2013**, *199*, 253−257.
(41) Klepov, V. V.; zur Loye, H.-C. Complex Topologies from Simple Building Blocks: Uranium(IV) Thiophosphates. *Inorg. Chem.* **2018**, *57*, 11175−11183.
(42) Juillerat, C. A.; Klepov, V. V.; Morrison, G.; Pace, K. A.; zur Loye, H.-C. Flux crystal growth: a versatile technique to reveal the crystal chemistry of complex uranium oxides. *Dalton Trans.* **2019**, *48*, 3162−3181.
(43) Malliakas, C. D.; Yao, J.; Wells, D. M.; Jin, G. B.; Skanthakumar, S.; Choi, E. S.; Balasubramanian, M.; Soderholm, L.; Ellis, D. E.; Kanatzidis, M. G.; Ibers, J. A. Oxidation State of Uranium in $A_6Cu_{12}U_2S_{15}$ (A = K, Rb, Cs) Compounds. *Inorg. Chem.* **2012**, *51*, 6153−6163.
(44) Mesbah, A.; Prakash, J.; Beard, J. C.; Pozzi, E. A.; Tarasenko, M. S.; Lebègue, S.; Malliakas, C. D.; Van Duyne, R. P.; Ibers, J. A. Positional flexibility: syntheses and characterization of six uranium chalcogenides related to the 2H hexagonal perovskite family. *Inorg. Chem.* **2015**, *54*, 2851−2857.
(45) Ward, M. D.; Ibers, J. A. The Synthesis and Crystal Structure of $U_7O_2Se_{12}$. *Z. Anorg. Allg. Chem.* **2014**, *640*, 1585−1588.
(46) Kohlmann, H.; Beck, H. P. Synthesis and Crystal Structure of the γ-Modifications of US_2 and USe_2. *Z. Anorg. Allg. Chem.* **1997**, *623*, 785−790.
(47) Unruh, C. M. *Transuranium Radionuclides. A Manual of Good Practice*. No. BNWL-SA-3075 (DRAFT); Battelle Pacific Northwest Labs.: Richland, USA, 1970.
(48) Windorff, C. J.; Beltran-Leiva, M. J.; Albrecht-Schönzart, T. E.; Bai, Z.; Celis-Barros, C.; Goodwin, C. A. P.; Huffman, Z.; McKinnon, N. C.; Sperling, J. M. Synthesis, characterization, and theoretical analysis of a plutonyl phosphine oxide complex. *Dalton Trans.* **2021**, *50*, 14537−14541.
(49) Su, J.; Cheisson, T.; McSkimming, A.; Goodwin, C. A. P.; DiMucci, I.; Albrecht-Schönzart, T.; Scott, B. L.; Batista, E. R.; Gaunt, A. J.; Kozimor, S. A.; Yang, P.; Schelter, E. J. Complexation and redox chemistry of neptunium, plutonium and americium with a hydroxylaminato ligand. *Chem. Sci.* **2021**, *12*, 13343−13359.
(50) Borschel, G. H.; Lounsbury, M. W.; Lopez, J. J.; Burke, L. L.; Case, R. L.; Johnston, J. D.; Cannon, J. A.; Borland, M. W. *AFCI Glovebox Radiological Release-Evaluation, Corrective Actions and Testing*. No. INL/EXT-15-36996-Rev000; Idaho National Lab. (INL): Idaho Falls, USA, 2015.
(51) Breton, L. S.; Klepov, V. V.; zur Loye, H.-C. Facile Oxide to Chalcogenide Conversion for Actinides Using the Boron-Chalcogen Mixture Method. *J. Am. Chem. Soc.* **2020**, *142*, 14365−14373.
(52) Li, Y.-Y.; Liu, P.-F.; Wu, L.-M. $Ba_6Zn_7Ga_2S_{16}$: A Wide Band Gap Sulfide with Phase-Matchable Infrared NLO Properties. *Chem. Mater.* **2017**, *29*, 5259−5266.
(53) Zhang, M.-J.; Jiang, X.-M.; Zhou, L.-J.; Guo, G.-C. Two phases of Ga_2S_3: promising infrared second-order nonlinear optical materials with very high laser induced damage thresholds. *J. Mater. Chem. C* **2013**, *1*, 4754.
(54) Wu, L. M.; Seo, D. K. New solid-gas metathetical synthesis of binary metal polysulfides and sulfides at intermediate temperatures: utilization of boron sulfides. *J. Am. Chem. Soc.* **2004**, *126*, 4676−4681.
(55) Ma, N.; Li, F.; Li, J.-G.; Liu, X.; Zhang, D.-B.; Li, Y.-Y.; Chen, L.; Wu, L.-M. Mixed-Valence $CsCu_4Se_3$: Large Phonon Anharmo-

https://doi.org/10.1021/jacs.2c04783
J. Am. Chem. Soc. 2022, 144, 13773−13786

nicity Driven by the Hierarchy of the Rigid $[(Cu^{+})_4(Se^{2-})_2](Se^{-})$ Double Anti-CaF_2 Layer and the Soft Cs^{+} Sublattice. *J. Am. Chem. Soc.* **2021**, *143*, 18490−18501.
(56) Koscielski, L. A.; Ibers, J. A. The Structural Chemistry of Quaternary Chalcogenides of the Type AMM'Q_3. *Z. Anorg. Allg. Chem.* **2012**, *638*, 2585−2593.
(57) Pal, K.; Xia, Y.; Shen, J.; He, J.; Luo, Y.; Kanatzidis, M. G.; Wolverton, C. Accelerated discovery of a large family of quaternary chalcogenides with very low lattice thermal conductivity. *npj Comput. Mater.* **2021**, *7*, 82.
(58) Vergniory, M. G.; Elcoro, L.; Felser, C.; Regnault, N.; Bernevig, B. A.; Wang, Z. A complete catalogue of high-quality topological materials. *Nature* **2019**, *566*, 480−485.
(59) Mansuetto, M. F.; Keane, P. M.; Ibers, J. A. Synthesis and structures of the new group IV chalcogenides $NaCuTiS_3$ and $NaCuZrQ_3$ (Q= S, Se, Te). *J. Solid State Chem.* **1993**, *105*, 580−587.
(60) Kanatzidis, M. G. Discovery-Synthesis, Design, and Prediction of Chalcogenide Phases. *Inorg. Chem.* **2017**, *56*, 3158−3173.
(61) Klepov, V. V.; Smith, M. D.; zur Loye, H. C. Targeted Synthesis of Uranium(IV) Thiosilicates. *Inorg. Chem.* **2019**, *58*, 8275−8278.
(62) Klepov, V. V.; Pace, K. A.; Breton, L. S.; Kocevski, V.; Besmann, T. M.; zur Loye, H.-C. Nearly Identical but Not Isotypic: Influence of Lanthanide Contraction on $Cs_2NaLn(PS_4)_2$ (Ln = La−Nd, Sm, and Gd−Ho). *Inorg. Chem.* **2020**, *59*, 1905−1916.
(63) Sutorik, A. C.; Kanatzidis, M. G. Reactions of Lanthanides and Actinides in Molten Alkali Metal/Polychalcogenide Fluxes at Intermediate Temperatures (250− 600° C). *Chem. Mater.* **1997**, *9*, 387−398.
(64) Klepov, V. V.; Kocevski, V.; Besmann, T. M.; zur Loye, H.-C. Dimensional reduction upon calcium incorporation in $Cs_{0.3}(Ca_{0.3}Ln_{0.7})PS_4$ and $Cs_{0.5}(Ca_{0.5}Ln_{0.5})PS_4$. *CrystEngComm* **2021**, *23*, 831−840.
(65) Kutahyali Aslani, C.; Breton, L. S.; Klepov, V. V.; zur Loye, H.-C. A series of $Rb_4Ln_2(P_2S_6)(PS_4)_2$ (Ln = La, Ce, Pr, Nd, Sm, Gd) rare earth thiophosphates with two distinct thiophosphate units $[P^{V}S_4]^{3-}$ and $[P^{IV}{}_2S_6]^{4-}$. *Dalton Trans.* **2021**, *50*, 1683−1689.
(66) Ayer, G. B.; Klepov, V. V.; Pace, K. A.; zur Loye, H.-C. Quaternary cerium(iv) containing fluorides exhibiting Ce_3F_{16} sheets and Ce_6F_{30} frameworks. *Dalton Trans.* **2020**, *49*, 5898−5905.
(67) Ruseikina, A. V.; Chernyshev, V. A.; Velikanov, D. A.; Aleksandrovsky, A. S.; Shestakov, N. P.; Molokeev, M. S.; Grigoriev, M. V.; Andreev, O. V.; Garmonov, A. A.; Matigorov, A. V.; Melnikova, L. V.; Kislitsyn, A. A.; Volkova, S. S. Regularities of the property changes in the compounds $EuLnCuS_3$ (Ln= La-Lu). *J. Alloys Compd.* **2021**, *874*, 159968.
(68) Azarapin, N. O.; Aleksandrovsky, A. S.; Atuchin, V. V.; Gavrilova, T. A.; Krylov, A. S.; Molokeev, M. S.; Mukherjee, S.; Oreshonkov, A. S.; Andreev, O. V. Synthesis, structural and spectroscopic properties of orthorhombic compounds $BaLnCuS_3$ (Ln = Pr, Sm). *J. Alloys Compd.* **2020**, *832*, 153134.
(69) Kirklin, S.; Saal, J. E.; Meredig, B.; Thompson, A.; Doak, J. W.; Aykol, M.; Rühl, S.; Wolverton, C. The Open Quantum Materials Database (OQMD): assessing the accuracy of DFT formation energies. *npj Comput. Mater.* **2015**, *1*, 15010.
(70) Saal, J. E.; Kirklin, S.; Aykol, M.; Meredig, B.; Wolverton, C. Materials Design and Discovery with High-Throughput Density Functional Theory: The Open Quantum Materials Database (OQMD). *JOM* **2013**, *65*, 1501−1509.
(71) Selby, H. D.; Chan, B. C.; Hess, R. F.; Abney, K. D.; Dorhout, P. K. Three New Phases in the K/Cu/Th/S System: $KCuThS_3$, $K2Cu_2ThS_4$, and $K_3Cu_3Th_2S_7$. *Inorg. Chem.* **2005**, *44*, 6463−6469.
(72) Wells, D. M.; Jin, G. B.; Skanthakumar, S.; Haire, R. G.; Soderholm, L.; Ibers, J. A. Quaternary Neptunium Compounds: Syntheses and Characterization of $KCuNpS_3$, $RbCuNpS_3$, $CsCuNpS_3$, $KAgNpS_3$, and $CsAgNpS_3$. *Inorg. Chem.* **2009**, *48*, 11513−11517.
(73) Yao, J.; Wells, D. M.; Chan, G. H.; Zeng, H. Y.; Ellis, D. E.; Van Duyne, R. P.; Ibers, J. A. Syntheses, structures, physical properties, and electronic properties of some $AMUQ_3$ compounds (A = alkali metal, M = Cu or Ag, Q = S or Se). *Inorg. Chem.* **2008**, *47*, 6873−6879.
(74) Sutorik, A. C.; Albritton-Thomas, J.; Hogan, T.; Kannewurf, C. R.; Kanatzidis, M. G. New Quaternary Compounds Resulting from the Reaction of Copper and f-Block Metals in Molten Polychalcogenide Salts at Intermediate Temperatures. Valence Fluctuations in the Layered $CsCuCeS_3$. *Chem. Mater.* **1996**, *8*, 751−761.
(75) Huang, F. Q.; Mitchell, K.; Ibers, J. A. New layered materials: syntheses, structures, and optical and magnetic properties of $CsGdZnSe_3$, $CsZrCuSe_3$, $CsUCuSe_3$, and $BaGdCuSe_3$. *Inorg. Chem.* **2001**, *40*, 5123−5126.
(76) Narducci, A. A.; Ibers, J. A. The related compounds $MThTe_3$ (M = Mn, Mg) and $ACuThSe_3$ (A = K, Cs): syntheses and characterization. *Inorg. Chem.* **2000**, *39*, 688−691.
(77) (a) Klepov, V. V.; Berseneva, A. A.; Pace, K. A.; Kocevski, V.; Sun, M.; Qiu, P.; Wang, H.; Chen, F.; Besmann, T. M.; Zur Loye, H. C. $NaGaS_2$: An Elusive Layered Compound with Dynamic Water Absorption and Wide-Ranging Ion-Exchange Properties. *Angew. Chem., Int. Ed.* **2020**, *59*, 10836−10841. (b) Klepov, V. V.; Berseneva, A. A.; Pace, K. A.; Kocevski, V.; Sun, M.; Qiu, P.; Wang, H.; Chen, F.; Besmann, T. M.; Zur Loye, H. C. $NaGaS_2$: An Elusive Layered Compound with Dynamic Water Absorption and Wide-Ranging Ion-Exchange Properties. *Angew. Chem.* **2020**, *132*, 10928−10933.
(78) Adhikary, A.; Yaghoobnejad Asl, H.; Sandineni, P.; Balijapelly, S.; Mohapatra, S.; Khatua, S.; Konar, S.; Gerasimchuk, N.; Chernatynskiy, A. V.; Choudhury, A. Unusual Atmospheric Water Trapping and Water Induced Reversible Restacking of 2D Gallium Sulfide Layers in $NaGaS_2$ Formed by Supertetrahedral Building Unit. *Chem. Mater.* **2020**, *32*, 5589−5603.
(79) Smith, D. W. Ionic hydration enthalpies. *J. Chem. Educ.* **1977**, *54*, 540.
(80) Choi, K.-S.; Kanatzidis, M. G. New Uranium Chalcoantimonates, RbU_2SbS_8 and KU_2SbSe_8, with a Polar Noncentrosymmetric Structure. *Chem. Mater.* **1999**, *11*, 2613−2618.
(81) Mizoguchi, H.; Gray, D.; Huang, F. Q.; Ibers, J. A. Structures and bonding in $K_{0.91}U_{1.79}S_6$ and KU_2Se_6. *Inorg. Chem.* **2006**, *45*, 3307−3311.
(82) Clifton, J. R.; Gruen, D. M.; Ron, A. Electronic Absorption Spectra of Matrix-Isolated Uranium Tetrachloride and Uranium Tetrabromide Molecules. *J. Chem. Phys.* **1969**, *51*, 224−232.
(83) Schoenes, J. Electronic transitions, crystal field effects and phonons in UO_2. *Phys. Rep.* **1980**, *63*, 301−336.
(84) Su, J.; Batista, E. R.; Boland, K. S.; Bone, S. E.; Bradley, J. A.; Cary, S. K.; Clark, D. L.; Conradson, S. D.; Ditter, A. S.; Kaltsoyannis, N.; Keith, J. M.; Kerridge, A.; Kozimor, S. A.; Löble, M. W.; Martin, R. L.; Minasian, S. G.; Mocko, V.; La Pierre, H. S.; Seidler, G. T.; Shuh, D. K.; Wilkerson, M. P.; Wolfsberg, L. E.; Yang, P. Energy-Degeneracy-Driven Covalency in Actinide Bonding. *J. Am. Chem. Soc.* **2018**, *140*, 17977−17984.
(85) Bergstrom, F. W. The Polysulfides and Polyselenides of Lithium, Sodium and Potassium. *J. Am. Chem. Soc.* **1926**, *48*, 146−151.
(86) Spek, A. L. PLATONSQUEEZE: a tool for the calculation of the disordered solvent contribution to the calculated structure factors. *Acta Crystallogr., Sect. C: Struct. Chem.* **2015**, *71*, 9−18.
(87) Ravel, B.; Newville, M. ATHENA, ARTEMIS, HEPHAESTUS: data analysis for X-ray absorption spectroscopy using IFEFFIT. *J. Synchrotron Radiat.* **2005**, *12*, 537−541.
(88) Kresse, G.; Furthmüller, J. Efficiency of ab-initio total energy calculations for metals and semiconductors using a plane-wave basis set. *J. Comput. Mater. Sci.* **1996**, *6*, 15−50.
(89) Kresse, G.; Furthmüller, J. Efficient iterative schemes for ab initio total-energy calculations using a plane-wave basis set. *Phys. Rev. B: Condens. Matter Mater. Phys.* **1996**, *54*, 11169−11186.
(90) Kresse, G.; Joubert, D. From ultrasoft pseudopotentials to the projector augmented-wave method. *Phys. Rev. B: Condens. Matter Mater. Phys.* **1999**, *59*, 1758−1775.

https://doi.org/10.1021/jacs.2c04783
J. Am. Chem. Soc. 2022, 144, 13773−13786

(91) Perdew, J. P.; Burke, K.; Ernzerhof, M. Generalized Gradient Approximation Made Simple. *Phys. Rev. Lett.* **1996**, *77*, 3865−3868.
(92) Setyawan, W.; Curtarolo, S. High-throughput electronic band structure calculations: Challenges and tools. *J. Comput. Mater. Sci.* **2010**, *49*, 299−312.
(93) Henkelman, G.; Arnaldsson, A.; Jónsson, H. A fast and robust algorithm for Bader decomposition of charge density. *J. Comput. Mater. Sci.* **2006**, *36*, 354−360.
(94) Tang, W.; Sanville, E.; Henkelman, G. A grid-based Bader analysis algorithm without lattice bias. *J. Phys.: Condens. Matter* **2009**, *21*, 084204.
(95) Grimme, S. Semiempirical GGA-type density functional constructed with a long-range dispersion correction. *J. Comput. Chem.* **2006**, *27*, 1787−1799.
(96) Vitova, T.; Pidchenko, I.; Fellhauer, D.; Bagus, P. S.; Joly, Y.; Pruessmann, T.; Bahl, S.; Gonzalez-Robles, E.; Rothe, J.; Altmaier, M.; Denecke, M. A.; Geckeis, H. The role of the 5f valence orbitals of early actinides in chemical bonding. *Nat. Commun.* **2017**, *8*, 16053.
(97) Heyd, J.; Scuseria, G. E.; Ernzerhof, M. Hybrid functionals based on a screened Coulomb potential. *J. Chem. Phys.* **2003**, *118*, 8207−8215.
(98) Anisimov, V. I.; Zaanen, J.; Andersen, O. K. Band theory and Mott insulators: HubbardUinstead of StonerI. *Phys. Rev. B: Condens. Matter Mater. Phys.* **1991**, *44*, 943−954.
(99) Pegg, J. T.; Aparicio-Anglès, X.; Storr, M.; de Leeuw, N. H. DFT+U study of the structures and properties of the actinide dioxides. *J. Nucl. Mater.* **2017**, *492*, 269−278.

https://doi.org/10.1021/jacs.2c04783
J. Am. Chem. Soc. 2022, 144, 13773−13786